Investigations on vortex evolution and wake dynamics of bio-inspired pitching hydrofoils

Yefang Wang[1], Lei Shi[1,2,a], Annie-Claude Bayeul-Lainé[2], Olivier Coutier-Delgosha[2,3]

[1]Research Center of Fluid Machinery Engineering and Technology, Jiangsu University, Zhenjiang 212013, China

[2]Univ. Lille, CNRS, ONERA, Arts et Métiers ParisTech, Centrale Lille, UMR 9014 - LMFL - Laboratoire de Mécanique des Fluides de Lille - Kampé de Feriet, F-59000 Lille, France

[3]Kevin T. Crofton Department of Aerospace and Ocean Engineering, Virginia Tech, Blacksburg, VA 24060, USA

[a]Corresponding E-mail: Lei.shi@ensam.eu

Abstract

Recently, lots of oscillating targets inspired from motions of some insects and birds have been applied extensively to many engineering applications. The aim of this work is to reveal the performance and detailed flow structures over the pitching corrugated hydrofoils under various working conditions, using the SST $\gamma - \widetilde{Re}_\theta$ transition model. First of all, the lift coefficients of a smooth oscillating airfoil at different reduced frequency and pitching angles show a good agreement with the experiments, characterized by the accurate prediction of the light and deep stall. For the pitching corrugated hydrofoils, it shows that the mean lift coefficient increases with the pitching magnitude, but it has an obvious drop at high reduced frequency for the case with large pitching amplitude, which is mainly induced by the pressure modification on the surface with smooth curvature, depending on the oscillation significantly. In addition, the mean drag coefficient also indicates that the drag turns into the thrust at high reduced frequency when the pitching amplitude exceeds to the value of $10°$. Increasing the reduced frequency delays the flow structure and leads to the deflection of the wake vortical flow. The Reynold number also has an impact on the hydrofoil performance and wake morphology. Furthermore, regarding the shape effect, it seems that hydrofoil A (consisting of two protrusions and hollows and the aft part with smooth curvature) achieves the higher lift than hydrofoil B (comprising several protrusions and hollows along the surface), specially at high reduced frequency. Although the frequency collected from two hydrofoils remains nearly the same near the leading edge and in the wake region, the high sub-frequency is evidently reduced for hydrofoil B in second and third

hollows, due to the relatively stable trapped vortices. Then, the wake transition from the thrust-indicative to drag-indicative profile for hydrofoil B is also slower compared with hydrofoil A. Finally, it is observed that with the increase of the thickness, the lift/drag ratio decreases and the slow wake transition is detected for the thin hydrofoil, which is associated with the relatively low drag coefficient.

Keywords: numerical simulation; corrugated pitching hydrofoils; reduced frequency; Reynolds number; hydrofoil thickness

1. Introduction

The inspiration of a better design of some underwater propulsion system and micro air vehicles (MAVs), is mainly from the natural insect wings and insect flight mechanics. Therefore, it is not surprising that there is an urgent of interest in investigating for the lift generation or stall mitigation. Except for exploring how the exact oscillating mechanisms employed by insects contribute toward the agility during flight, understanding how the especial surface geometry and features of their wings enable the insects to maneuver the way they do is also a major topic of debate for some recent studies. Figure 1 shows the two-dimensional view of the dragonfly wing and the cross-section shapes. The cross sections are a row of the corrugated foils along the spanwise direction, therefore, it is really necessary to study the performance and unsteady vortical flows over different foils with various geometry.
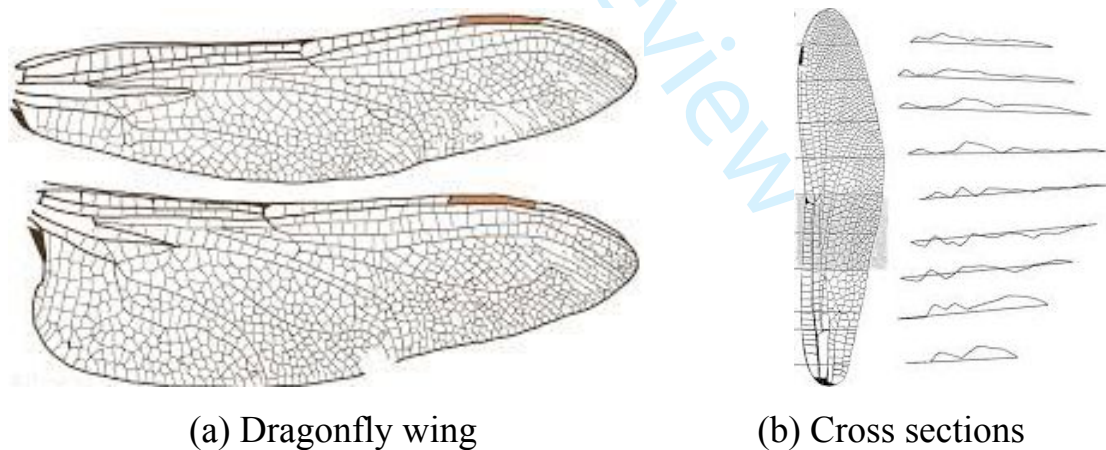

(a) Dragonfly wing   (b) Cross sections

Fig.1 Sketch of the dragonfly wings and the cross sections.

The motion mode of the oscillating foils can be mainly classified into three categories: plunging (or heaving), pitching and flapping (combination of heaving and pitching motions). Pitching motion is a simple kinematic that the objective rotates around a torsion point in a limited range of incidences. In the oscillating period, the target would have the modifications of the blade loading, from the

relatively small incidence (due to the laminar-turbulence transition effect) to the large one (mainly induced by the flow separation). Many related works regarding the flow structures of pitching foils have been conducted previously and much progress have been made. Tseng and Hu [1] detected the sources of some special vortex structures using the Lagrangian coherent structure (LCS) for a pitching airfoil. Then, Tseng and Cheng revealed the mechanism of the stall delay at different stages and the results show that the postponed stall is strongly associated with leading edge vortex (LEV) revolution. Ducoin et al. [3] employed the shear stress transport (SST) $\gamma - Re_{\theta t}$ transition model [4-5] to investigate the laminar-turbulence transition occurrence over a pitching hydrofoil and it is observed that the predicted wall pressure distribution has an acceptable agreement with the experiments. They also found that by increasing the pitching rate, not only does the stall delay, but also the transition is postponed and even suppressed for the highest pitching velocity during the pitch-up motion. Zhang et al. [6] concludes that the delayed stall is dependent of the first leading edge vortex and trailing edge vortex (TEV) for the high pitching velocity and the low pitching rate leads to the shrink of the hysteresis loops and intensive fluctuations of the dynamic force. Moubogha et al. [7] conducted the computations and experiments to study the flows around a pitching plate and the main conclusion is that the jet-like profiles of the wake are the main contributor to the thrust production. For the more complicated cavitating flows, Huang et al. [8] clarified the strong correlations between the cavity and vorticity structures, indicating that the evolution of sheet/cloud cavities are the main sources for vorticity production and modification. For the cases of pitching objective, the choice of turbulence is quite critical to the numerical accuracy. Although the advanced hybrid turbulence model is recommended [9] due to the three-dimensionality effect during the down-stroke process [10], the aforementioned study shows that the results are acceptable when the maximal pitching incidence is lower than 20° [11-12].

The corrugated foils exhibit different performance and flow structures compared with the smooth foils, in which the former is mainly induced by the pressure difference between the upper and lower surfaces. The previous work reported by Ho and New [13] shows that the corrugated hydrofoils can alleviate the massive flow separation and stall, which is proved by the particle image velocimetry (PIV) with the explanation that the protruding corners are acting as turbulators to generate vortices to promote the laminar-turbulence transition rapidly and the trapped vortex in the valleys can extract energy from the outside flows to the boundary layer to overcome the adverse pressure gradient [14]. Most of the early works focus on the global performance and vortex dynamics around the

stationary corrugated foils. For some specific examples, with the aid of PIV measurements, Murphy and Hu [15] observed that the aerodynamic performance of the smooth airfoil and flat plate vary considerably with the Reynolds number while the performance of the corrugated airfoil are insensitive to the Reynolds number. New et al. [16] compared the performance and vortex evolution among one smooth and two corrugated hydrofoils and the detailed information about how the geometry can influence the flow separation is demonstrated clearly. Furthermore, for the hydrofoil with an arc region, Levy and Seifert [17] stated that the flow separating from the corrugations would reattach on the aft-upper arc region, which is responsible for the reduction of the drag and lift enhancement due to the weak wake. When it comes to the pitching corrugated hydrofoils, Flint et al. [18] adopted the scale-adaptive simulation (SAS) to simulated the unsteady flows around a two-dimensional pitching corrugated hydrofoil and the main attention is paid to the effect of the pitching amplitude and reduced frequency on the performance prediction.

According to the previous study, it is observed that works on the corrugated foils are seldom performed, especially for the oscillating ones. In addition, the experiments have some difficulties in obtaining the flow structures near the surface. Therefore, as a complement, the goal of the present work is to conduct the simulations to the pitching corrugated hydrofoils, with main emphasis on the effect of the reduced frequency, Reynolds number, hydrofoil shape and thickness on the vortex dynamics and the resultant blade loading. The vortex evolution and wake dynamics of the pitching hydrofoils are described in detail under different working conditions. It is believed that this work can rich the understandings of the underlying physics of unsteady flows over rugged lifting profiles, which can provide some guidelines for a better design of underwater or aerial propulsive devices.

2. Turbulence modelling

2.1 Governing equations of SST k-ω model

The choice of the SST k-ω turbulence model in the present work is for the reason that it accounts for the transport of the turbulent shear stress and gives highly accurate prediction of the onset and the amount of flow separation under adverse pressure gradient [19]. It combines the standard k-ω model resolving the near-wall flow and standard k-ε model dealing with the outside free-stream flow by a blending function. The basic governing equations of SST k-ω model are given by

$$\frac{\partial(\rho k)}{\partial t} + \frac{\partial}{\partial x_j}(\rho u_j k) = P_k - D_k + \frac{\partial}{\partial x_j}\left((\mu + \sigma_k \mu_t)\frac{\partial k}{\partial x_j}\right) \tag{1}$$

4

$$\frac{\partial(\rho\omega)}{\partial t} + \frac{\partial}{\partial x_j}(\rho u_j \omega) = \alpha \frac{P_k}{\nu_t} - D_\omega + Cd_\omega + \frac{\partial}{\partial x_j}\left((\mu + \sigma_k \mu_t)\frac{\partial \omega}{\partial x_j}\right) \quad (2)$$

where P_k and D_k are the production and destruction terms in the turbulent kinetic energy equation. The eddy viscosity μ_t used to close the equations is calculated by

$$\mu_t = min\left[\frac{\rho k}{\omega}; \frac{a_1 \rho k}{SF_2}\right] \quad (3)$$

where S is the strain rate magnitude and F_2 is a blending function. The detailed information about the definitions and values of some parameters can be found in reference [19].

2.2 Governing equations of $\gamma - \widetilde{Re}_{\theta t}$ transition model

The introduction of the intermittency γ is to trigger the transition locally while the transition onset momentum thickness Reynolds number $\widetilde{Re}_{\theta t}$ is necessary to capture the nonlocal influence of the turbulence intensity. The main governing equations of $\gamma - \widetilde{Re}_{\theta t}$ model can be written as follows

$$\frac{\partial(\rho\gamma)}{\partial t} + \frac{\partial}{\partial x_j}(\rho u_j \gamma) = P_\gamma - E_\gamma + \frac{\partial}{\partial x_j}\left(\left(\mu + \frac{\mu_t}{\sigma_f}\right)\frac{\partial \gamma}{\partial x_j}\right) \quad (4)$$

$$\frac{\partial(\rho\widetilde{Re}_{\theta t})}{\partial t} + \frac{\partial}{\partial x_j}(\rho u_j \widetilde{Re}_{\theta t}) = P_{\theta t} + \frac{\partial}{\partial x_j}\left(\sigma_{\theta t}(\mu + \mu_t)\frac{\partial \widetilde{Re}_{\theta t}}{\partial x_j}\right) \quad (5)$$

where P_γ and E_γ are the source terms in intermittency equation while $P_{\theta t}$ is the source term in transition onset momentum thickness Reynolds number equation. The definitions of the correlations and magnitudes of constants in these two equations can refer to the reference [4-5].

2.3 Coupling of $\gamma - \widetilde{Re}_{\theta t}$ transition model with SST k-ω model

By the introduction of the effective intermittency γ_{eff}, the original source terms in turbulent kinetic energy equation are modified. The final formulation of k equation is shown by

$$\frac{\partial(\rho k)}{\partial t} + \frac{\partial}{\partial x_j}(\rho u_j k) = \tilde{P}_k - \tilde{D}_k + \frac{\partial}{\partial x_j}\left((\mu + \sigma_k \mu_t)\frac{\partial k}{\partial x_j}\right) \quad (6)$$

$$\tilde{P}_k = \gamma_{eff}P_k; \quad \tilde{D}_k = min\left(max\left(\gamma_{eff}, 0.1\right), 1.0\right)D_k \quad (7)$$

It is noted that the effective intermittency has no direct relationship with the eddy viscosity, which makes the equations solved relatively simply. In addition, there are two advantages should be stressed. The first one is the robustness of the model because the intermittency does not directly enter into the momentum equation. The other advantage is that the model has the capability to predict the effect of the high free stream turbulence level on buffeted laminar boundary

5

layers [5].

3. Computational configuration, meshing and boundary conditions

3.1 Computational domain and meshing

In this work, two different bio-inspired corrugated hydrofoils from reference [15] and [17] are employed to the two-dimensional flow simulation using the SST $\gamma - \widetilde{Re}_{\theta t}$ transition model under low Reynolds number condition. Corrugated hydrofoil A has two protrusions and two hollows, and the right part has the smooth curvature, while corrugated hydrofoil B is composed of several protrusions and hollows along the whole surface. Two tested targets have the same chord length c=75mm, which leads to the corresponding Reynolds number Re=1.4×10^4. The computational domain extends $5c$ from the hydrofoil leading edge and $15c$ from the trailing edge, which is enough due to the quick dissipation of the wake. Both the topwall and bottomwall have the same distance of $5c$ based on the rotating point. The hydrofoil rotates around a pivot-point which is located at x=0.25c from the leading edge and has a sinusoidal pitching motion of $\theta=\theta_0\sin(2\pi ft)$ (where θ is the pitching angle, θ_0 is the pitching amplitude and f is the pitching frequency).

(a)　　　　　　　　　　　　　　　　(b)
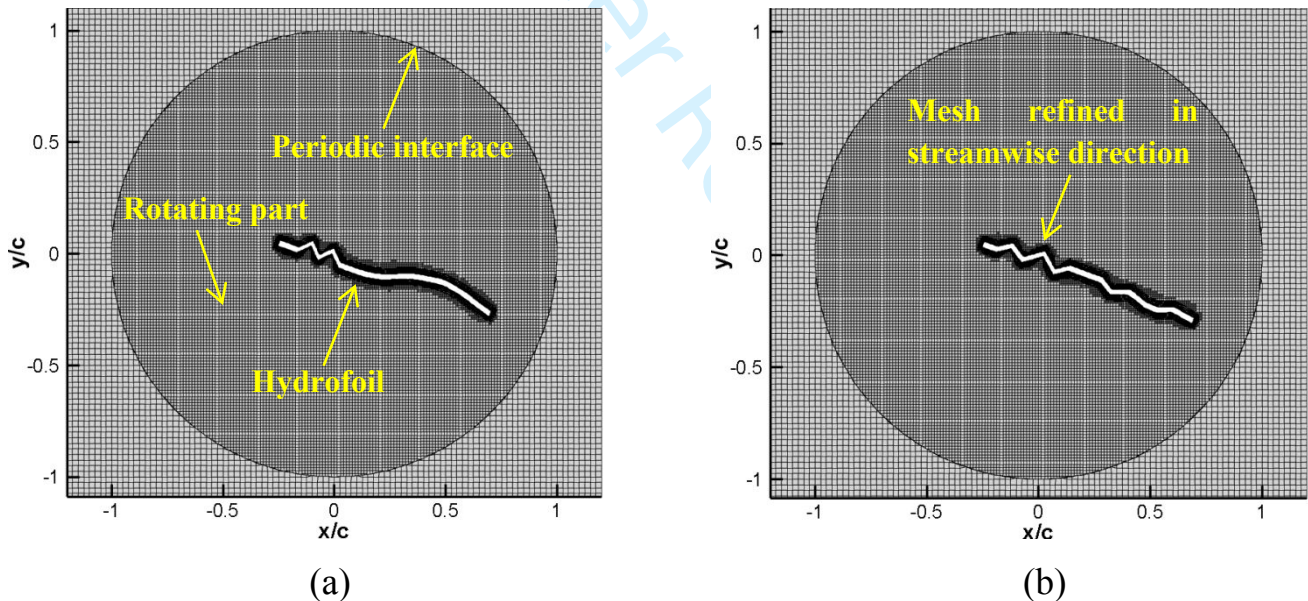
Fig.2 Computational domain and local mesh distributions. (b) Local mesh for corrugated hydrofoil A; (c) Local mesh for corrugated hydrofoil B.

The sliding mesh technique is used to control the sinusoidal motion of the pitching hydrofoils, by creating an interface between the stationary region and rotating part. The trimmed mesh is applied to the outside region while the prism layer is placed near the boundary layer. The total thickness of the prism layer is 2mm and the stretch ratio is 1.1, and the effect of the mesh near the wall is checked

by increasing the number of the prism layer. Simultaneously, the distribution of the mesh in the rotating part and near the hydrofoil surface are changed by decreasing the target size of the mesh. In order to capture the vortex shedding, a cylinder region including the rotating part and the wake is created and the internal mesh is also refined. The detailed information about the mesh refinement is described in table 1. Then, the y^+ distribution of mesh 2 for the hydrofoil at $20°$ is shown in figure 3. It can be seen that the maximal value exists near the leading edge and trailing edge due to the flow acceleration and flow separation, respectively. On the hydrofoil surface, the maximal magnitude of y^+ is always below 0.1. Then, the instantaneous lift coefficient ($C_l=F_l/(0.5*\rho*U_0^2*c)$, where F_l is the lift force, ρ is the density) and drag coefficient ($C_d= F_d/(0.5*\rho*U_0^2*c)$, where F_d is the drag force) in a rotating cycle obtained by different meshes are shown in figure 4. The tested target is hydrofoil A and the reduced frequency k_{red} is 1.28 ($k_{red}=\pi fc/U_0$), and the maximal pitching amplitude is $20°$. It seems that the lift and drag coefficients are noisy near the maximal positive and negative incidences as the hydrofoil undergoes the star-up and end-up process. However, it seems that the mesh has little difference to the results, especially for the mesh 2 and 3. In table 2, the time-averaged lift and drag coefficients obtained by different meshes are presented. The results indicate that the lift coefficient for mesh 3 has very small discrepancy compared with mesh 2, but the drag coefficient still increases with the mesh refinement due to the small value and the close relationship with the wall skin friction which is quite challenging to the RANS-based turbulence model. Consequently, with the consideration of the numerical accuracy and computational resource, the mesh 2 can be employed for all the tested cases.

Table 1 Detailed information about the mesh distribution

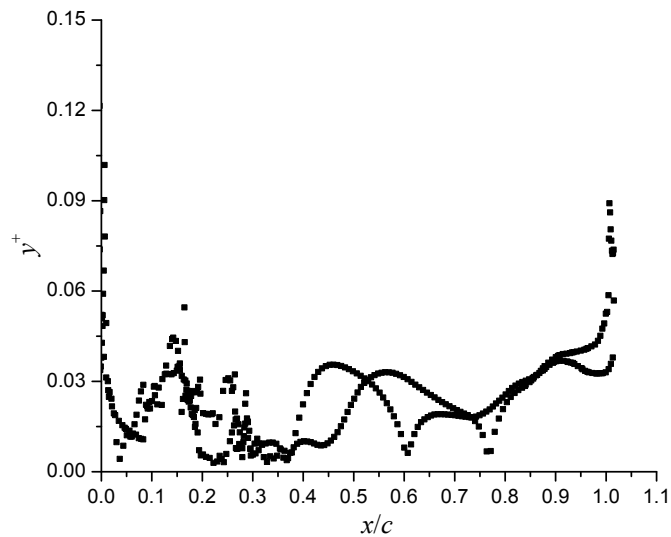|	Target size of the mesh in the rotating part (mm)	Number of the prism layer	Target size of the mesh near the hydrofoil surface (mm)	Mesh size in the wake region (mm)	Total cells
Mesh 1	1.5	70	1.0	2	154,043
Mesh 2	1.0	80	0.5	1.6	185,550
Mesh 3	0.75	90	0.4	1.5	209,219

7

Fig.3 Distribution of y^+ on corrugated hydrofoil A at maximal pitching angle.
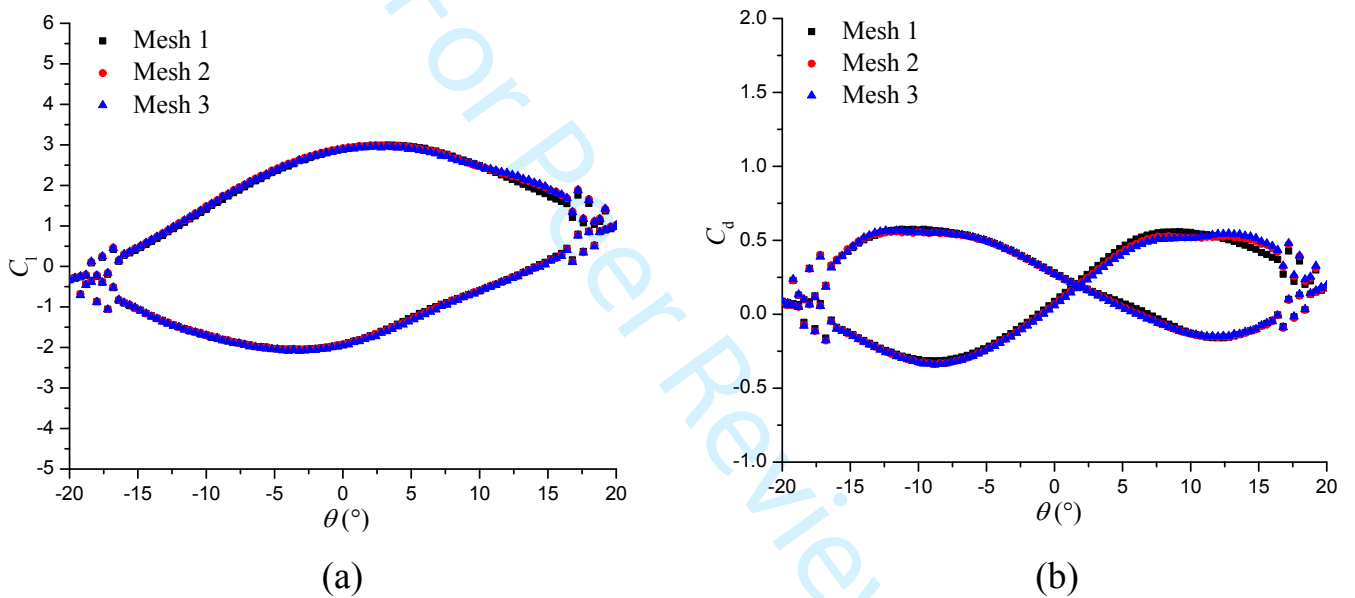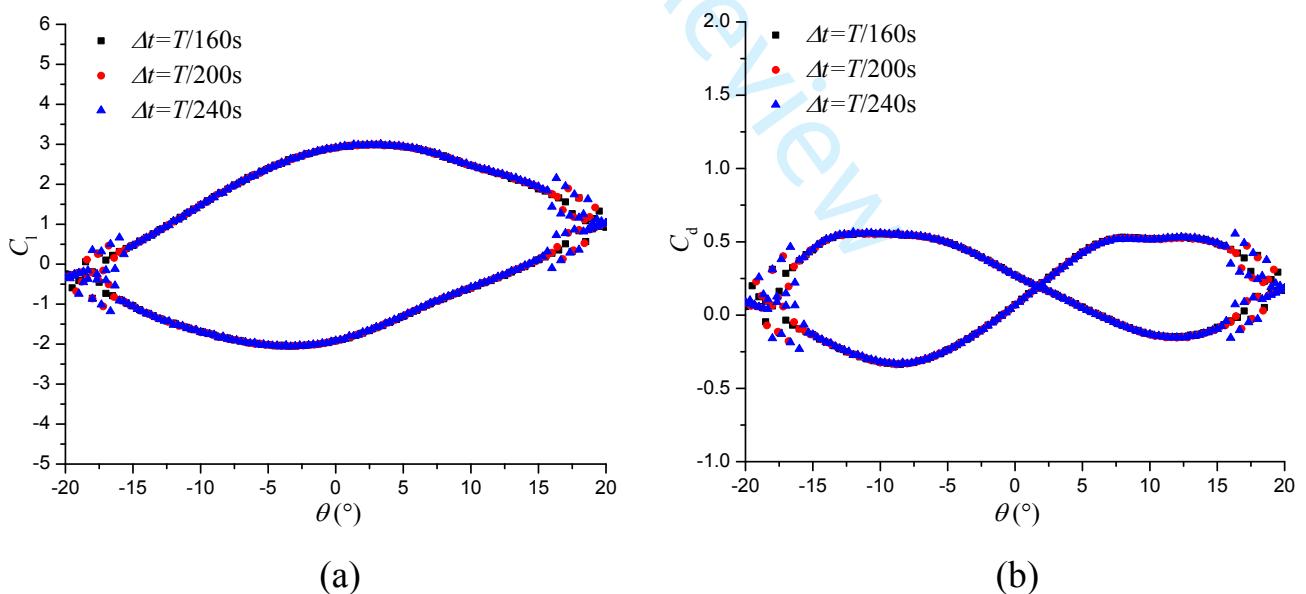

(a)

(b)

Fig.4 Instantaneous lift and drag coefficients for different meshes. (a) Lift coefficient; (b) Drag coefficient.

Table 2 Time-averaged lift and drag coefficients for different meshes

	C_l	Error (%)	C_d	Error (%)
Mesh 1	0.429	4.890	0.166	-1.190
Mesh 2	0.409	--	0.168	--
Mesh 3	0.410	0.244	0.170	1.190

3.2 Boundary conditions and numerical setup

When it comes to the boundary condition, the constant velocity U_0 is imposed on the inlet section while the pressure outlet is assigned on the outlet section. The topwall and bottomwall are set as the symmetry planes to eliminate any wall effect. The hydrofoil surface is regarded as the no-slip wall condition. The 2nd-order upwind scheme is applied to the convection term while the 2nd-order Backward Euler scheme is employed to the temporal discretization. The all y^+ wall treatment in STARCCM + code is employed, which is a hybrid treatment that attempts to emulate the high y^+ wall treatment for coarse meshes and the low y^+ wall treatment for fine meshes. It is also formulated with the desirable characteristic of producing reasonable answers for meshes of intermediate resolution. In addition, because the timestep has also great impact on the numerical results, as a result, three different timesteps, namely $T/160$s, $T/200$s and $T/240$s, are checked in the present work. The results of the instantaneous lift and drag coefficients in a revolution are displayed in figure 5. This is the case that the hydrofoil has a symmetrical pitching motion with the maximal amplitude of $20°$ and the reduced frequency of 1.28. It is observed that the timestep almost has no difference to the results. As shown in table 3, the time-averaged lift and drag coefficients obtained by $T/200$s and $T/240$s are quite close (error always below 0.5%). Finally, the timestep of $\Delta t = T/200$s is adopted to all the following cases.

(a)   (b)

Fig.5 Instantaneous lift and drag coefficients at different timesteps. (a) Lift coefficient; (b) Drag coefficient.

Table 3 Time-averaged lift and drag coefficients for different timesteps

9

	C_l	Error (%)	C_d	Error (%)
$\Delta t = T/160$s	0.4280	-0.2564	0.1665	-1.363
$\Delta t = T/200$s	0.4291	--	0.1688	--
$\Delta t = T/240$s	0.4292	0.02330	0.1684	0.2370

4. Results and discussion

4.1 Performance of an oscillating airfoil

Due to the limitation of the experiments about the oscillating corrugated foils, thus, the performance of an oscillating airfoil (NREL S809), mainly including the instantaneous lift coefficient at different reduced frequency and pitching angles, are displayed in the present work to validate the capability of the mesh and turbulence model. The experiments were performed in the NASA Ames 12.2m×24.4m wind tunnel. The Reynolds number is about 1×10^6 based on the freestream velocity and blade chord length, and the inlet turbulence level of the wind tunnel is about 0.1%. The detailed description of the experimental setup and measurements can be found in reference [20]. Based on the plotted curves in figure 6, it seems that the computational results can predict the light stall (smooth hysteresis loop) and deep stall (unstable hysteresis loop) accurately, as shown in figure 6d and 6e, respectively. With the increase of the reduced frequency, from figure 6b to 6d, the stall angle at the maximal lift coefficient is delayed, which is induced by the postponed separation of the flow structure. In addition, as the maximal pitching angle increases to $24°$, the discrepancy of the simulation with the experiment becomes relatively large, especially in the down-stroke process, where the three-dimensional effect can't be ignored [10]. Then, when it comes to the distribution of the drag coefficient in figure 6f, it is observed that the difference between the numerical and experimental results exist at the location where the hydrofoil has the maximal incidence. In general, it concludes that the numerical results show a good agreement with the experiments in the prediction of the lift and drag coefficients of the pitching airfoils.

10
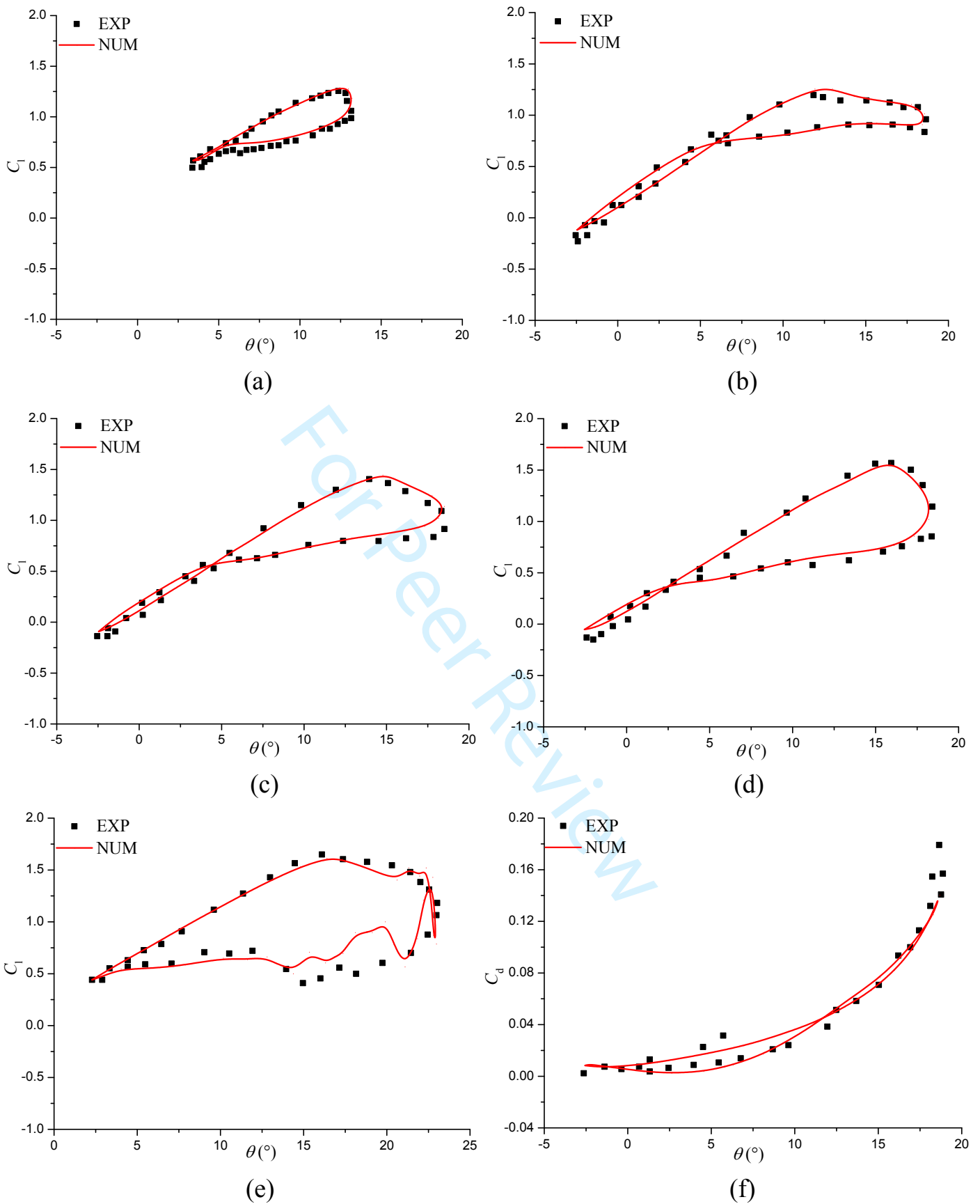
Fig.6 Instantaneous lift and drag coefficients in a revolution. (a) $\theta=8°+5.5°\sin(2\pi ft)$, $k_{red}=0.078$; (b) $\theta=8°+10°\sin(2\pi ft)$, $k_{red}=0.026$; (c) $\theta=8°+10°\sin(2\pi ft)$, $k_{red}=0.052$; (d) $\theta=8°+10°\sin(2\pi ft)$, $k_{red}=0.078$; (e) $\theta=14°+10°\sin(2\pi ft)$, $k_{red}=0.078$; (f) $\theta=8.05°+10.58°\sin(2\pi ft)$, $k_{red}=0.026$.

11

4.2 *General flow structure of corrugated hydrofoil A*

The general flow structure over hydrofoil A, characterized by the spanwise vorticity contours, is shown in figure 7. The tested case is the hydrofoil A with the thickness of 2mm, pitching amplitude of $10°$ and reduced frequency of 2.48. At initial time $t=t_1$, several discrete vortices with high negative vorticity emerge from the leading edge to the smooth curved surface, due to the flow separation and the existence of the protrusions and hollows. Additionally, the upper boundary layer flow sheds into the wake near the trailing edge. At the same time, on the lower surface, the high level of the positive vorticity occurs inside two hollows and the occurrence of vortex shedding is also evident on the aft part of the hydrofoil. At next time $t=t_2$ and t_3, as the hydrofoil experiences the pitch-down stage, the separated shear layer and vortices on the upper surface move totally away from the leading edge. Then, the shedding vortices near the trailing edge convect downstream. On the lower surface, the shear layer near the leading edge starts to separate and the separation point of the shear layer on the surface with smooth curvature moves upstream. Moreover, the boundary layer flow with the positive vorticity on the lower side begins to separate. Afterwards, the hydrofoil is at pitch-up stage from $t=t_4$ and t_5. At these two instants, the shedding vortices on the upper surface in previous time $t=t_3$ gradually disappear and a new shedding emerges, especially on the first protrusion. On the lower surface, the shear layer totally separates from the leading edge. Moreover, the boundary layer on the lower surface near the trailing edge also sheds the high level of the positive vorticity into the wakes. At last two instants $t=t_6$ and t_7, when the hydrofoil moves from a large incidence to a small one, the separated shear layer near the leading edge on the upper surface gradually weakens, which is opposite on the lower surface.
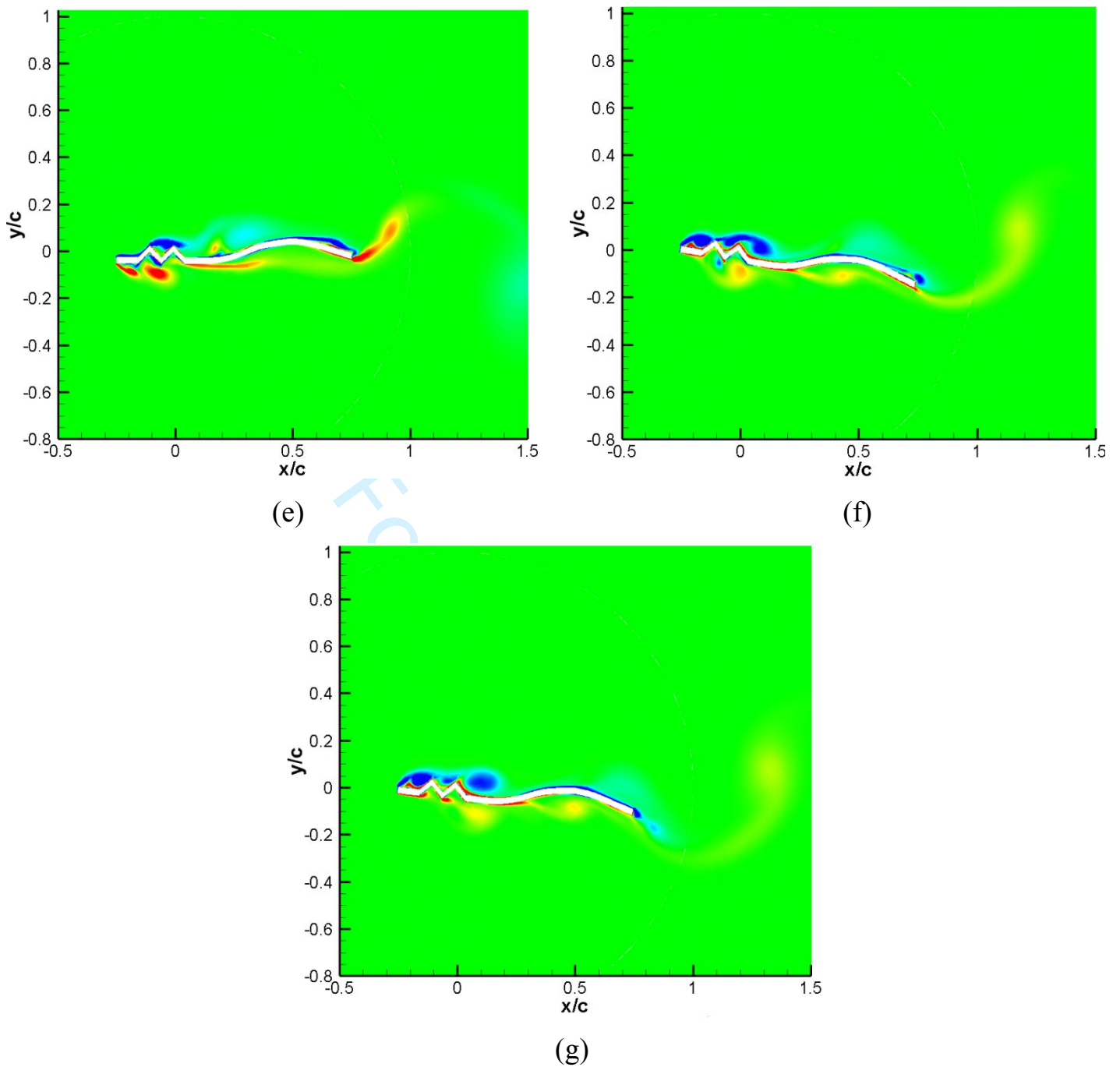
(a)

(b)

(c)

(d)

(e)

(f)

(g)
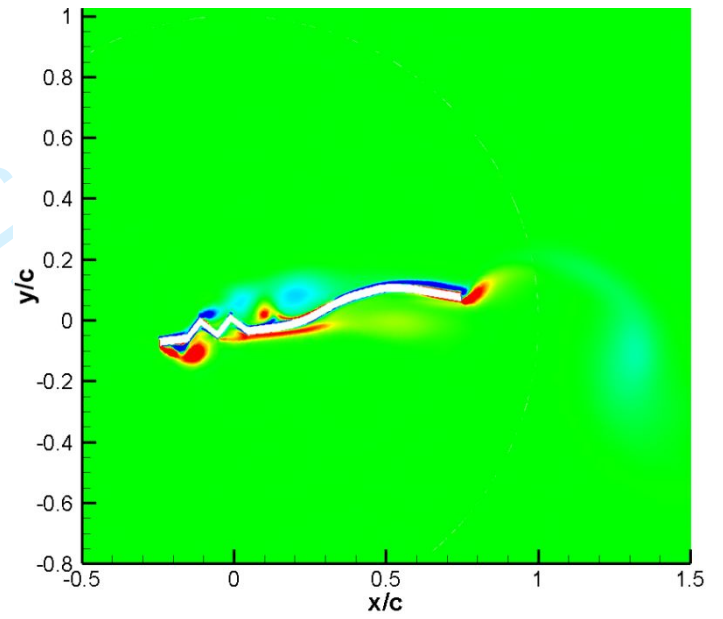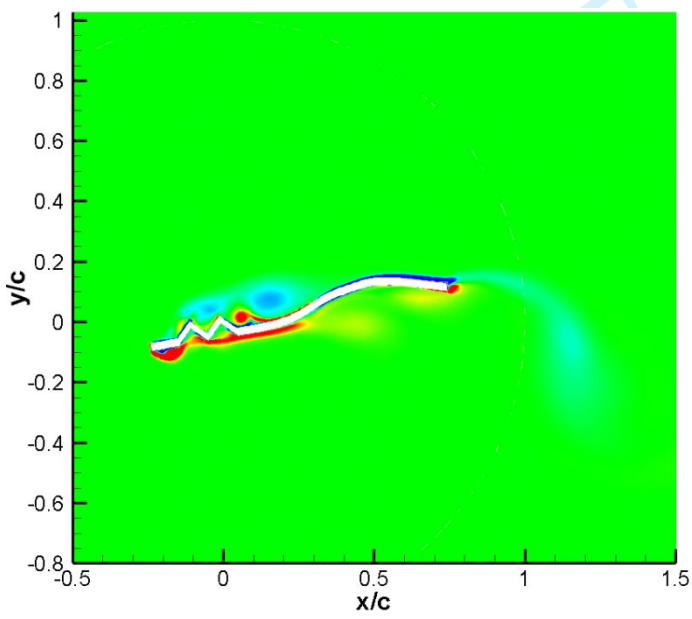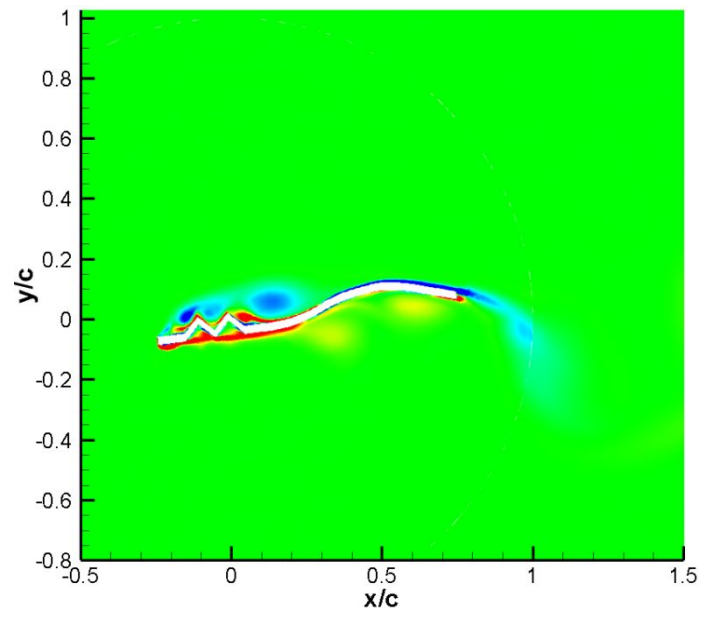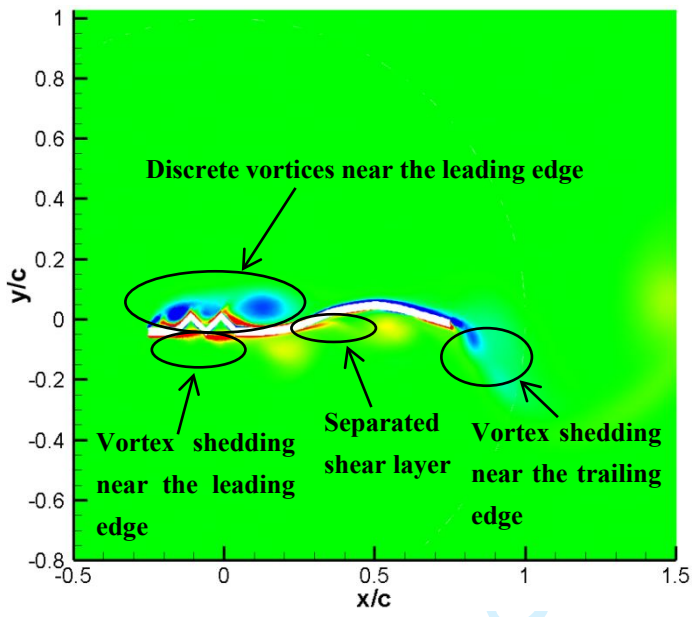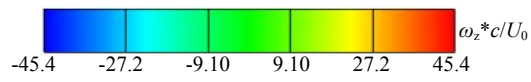
Fig.7 Instantaneous spanwise vorticity contours at different instants. (a) t_1; (b) t_2; (c) t_3; (d) t_4; (e) t_5; (f) t_6; (g) t_7.

To shed light on the flow structure near the hydrofoil surface in detail, the spanwise vorticity contours coupled with the relative streamlines at instant $t=t_1$ are shown in figure 8. Based on the figures, it is observed that there is a complex vortex system on the upper surface. The separation vortex A is generated due to the separated shear layer near the leading edge and a large-scale trapped vortex C is generated as the shear layer meets the first protrusion. Furthermore, it can be seen that an induced vortex B with high level of the positive vorticity emerges between the vortex A and C. Then, a trapped vortex D is created between the first protrusion

14

and second protrusion. After the second protrusion, the flow enters into the surface with the smooth curvature. A large-scale separation vortex F is captured, as well as an induced vortex E attached on the area between the vortex F and the second protrusion. On the lower surface, there is almost no flow separation near the leading edge, but two distinctive trapped vortex structures G and H are obvious. Near the trailing edge, as shown in figure 8b, there is the vortex street in the wake region induced by the alternate boundary layer separation due to the pitching motion. Generally, it concludes that the vortex structure over the corrugated hydrofoil is extremely complicated, which includes a series of the trapped and induced vortices, as well as the alternate shedding trailing edge vortex, leading to the performance change continuously.
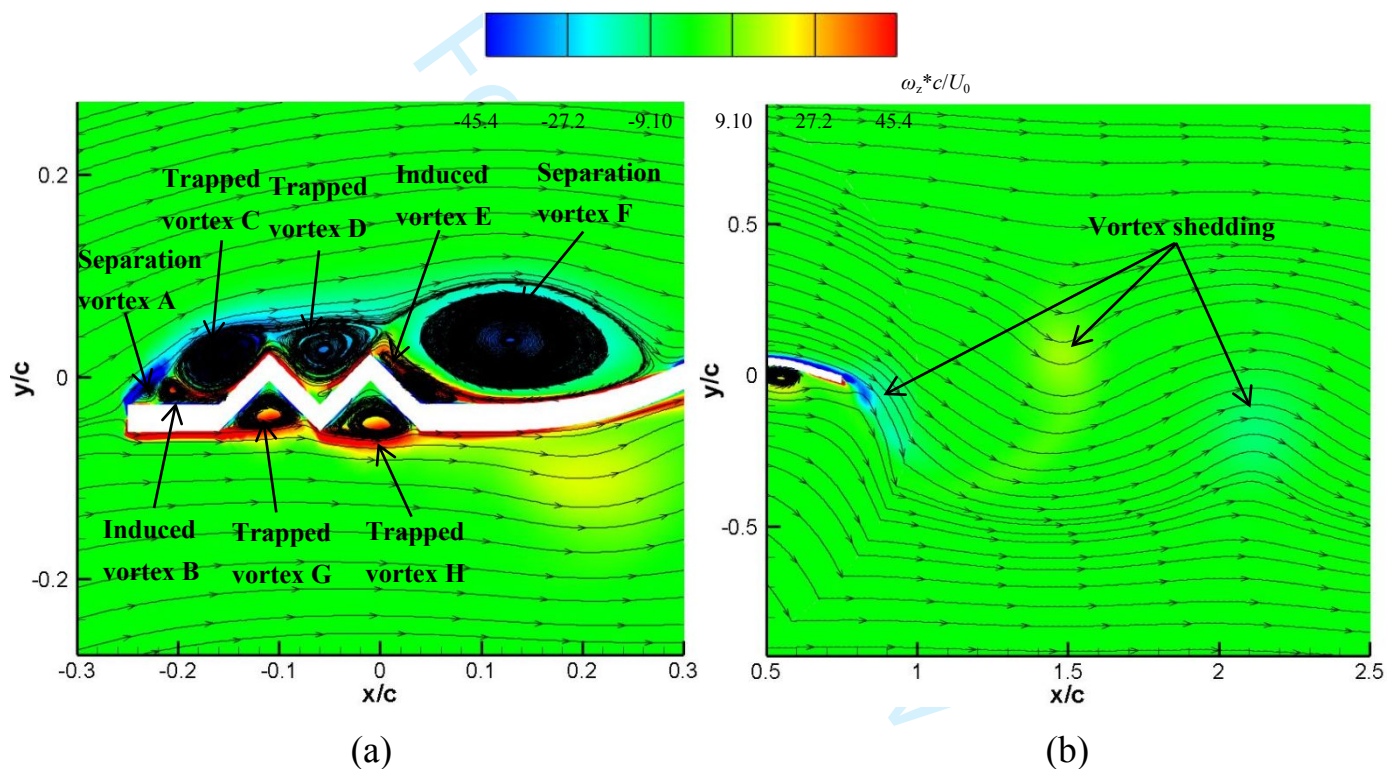
Fig.8 Near-wall and wake flow structure at instant $t=t_1$. (a) Over the hydrofoil surface; (b) In the wake region.

4.3 Effect of the pitching amplitude and reduced frequency

In this section, different pitching amplitudes and reduced frequency are tested to clarify the effect of vortex evolution on the change of lift and drag coefficients. The cases have the pitching amplitudes of 5°, 10° and 20° and reduced frequency of 1.24, 2.48 and 4.96. The target is corrugated hydrofoil A with the thickness of 2mm. In figure 9, the instantaneous and time-averaged lift and drag coefficients for various combinations of the pitching amplitude and reduced frequency are plotted. With the increase of the pitching amplitude, the predictive lift and drag coefficients

15

have large variation in a pitching cycle, but the change has the same trend when the reduced frequency remains unchanged. When considering the reduced frequency effect, it is observed that the maximal lift and drag coefficients have a shift with the increase of k_{red}. For an example, in figure 9a, 9c and 9e, the maximal negative lift coefficient shifts from a negative incidence (about -5°) to the positive one (about 5°) as the reduced frequency increases, while the maximal positive lift coefficient changes from the positive attack angle (about 5°) to a negative value (about -5°). Simultaneously, at k_{red}=4.96, the variation of drag coefficient is totally different and the maximal negative magnitude is at ±15° when the hydrofoil has the pitch-down motion. In figure 9g and 9h, the time-averaged results show that at the same reduced frequency, the lift coefficient increases with the incidence. However, when k_{red} increases to the value of 4.96, the lift coefficient of the hydrofoil at large incidence decreases significantly. For the distribution of the mean drag coefficient, it seems that it decreases evidently with the increase of k_{red} for the case with the large angle-of-attack, which indicates that the thrust is produced gradually. In this work, the cases of 10°-4.96, 20°-2.48 and 20°-4.96 can generate the propulsive force for the oscillating hydrofoils.
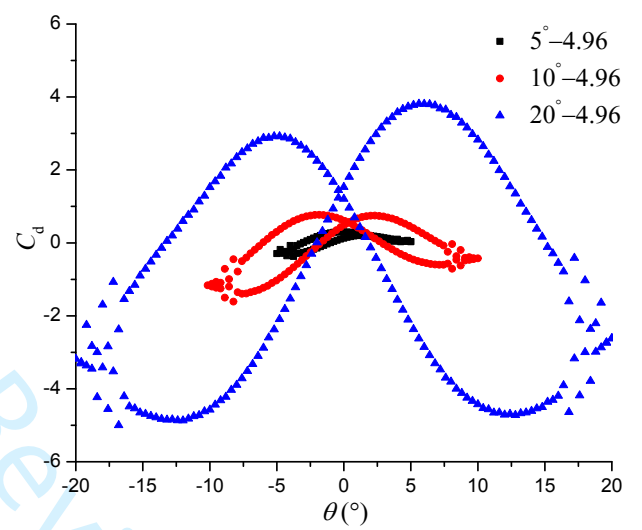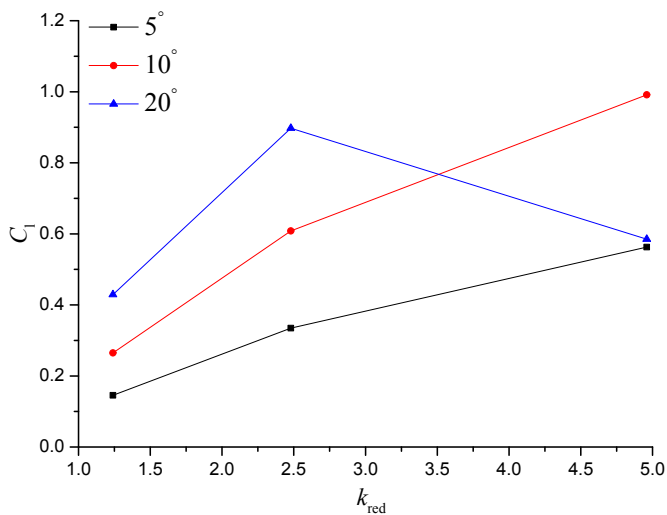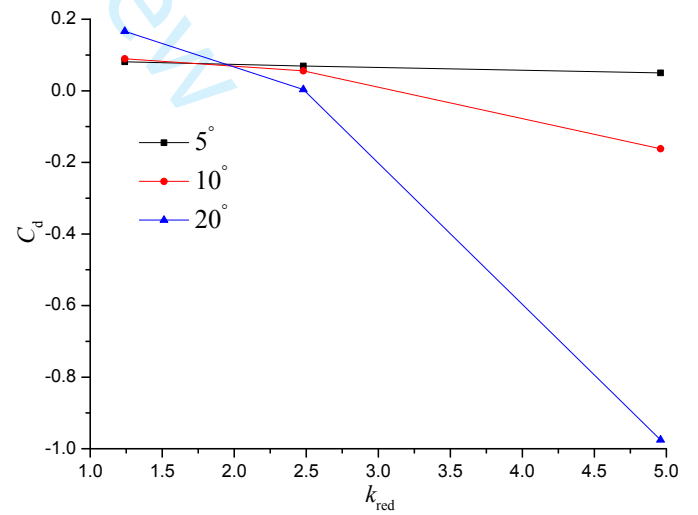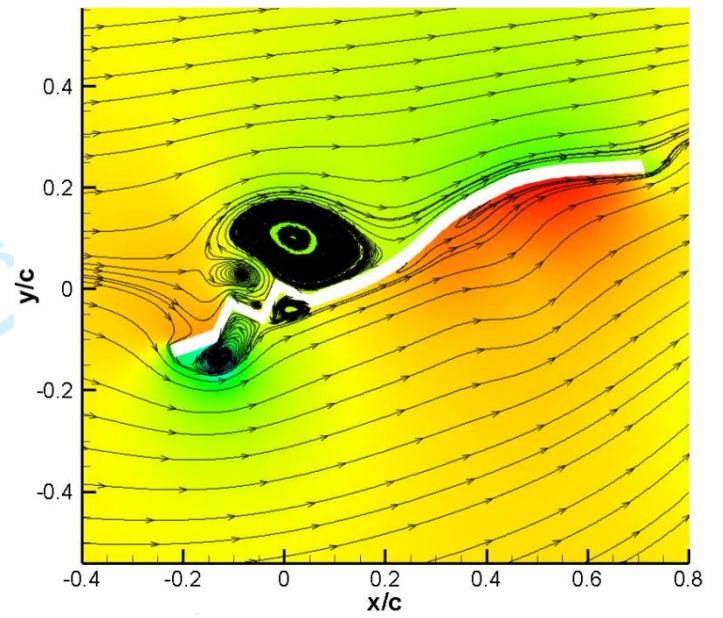

(a)
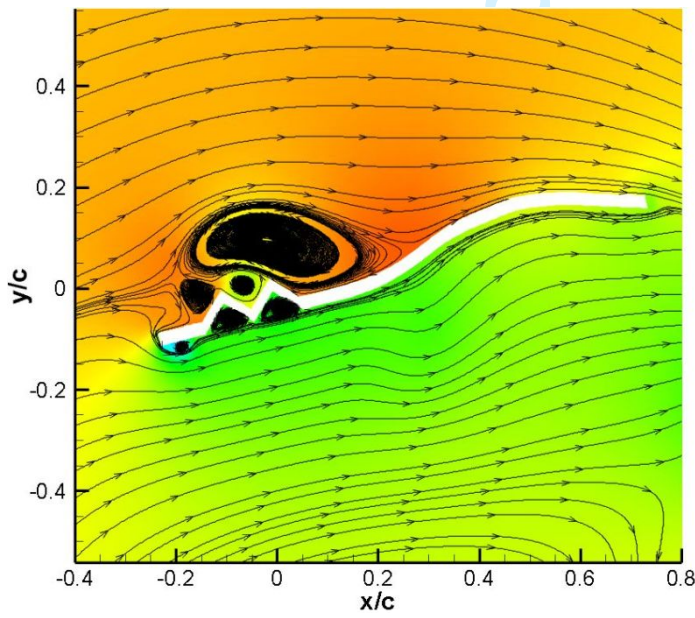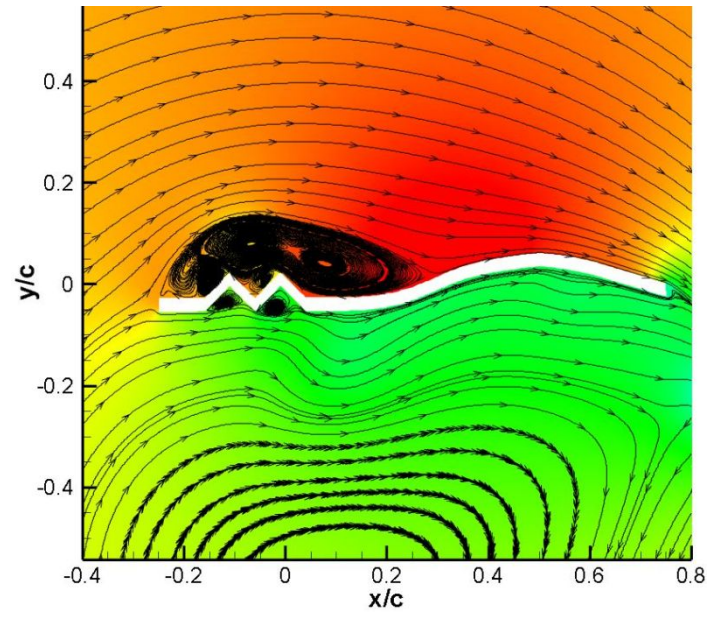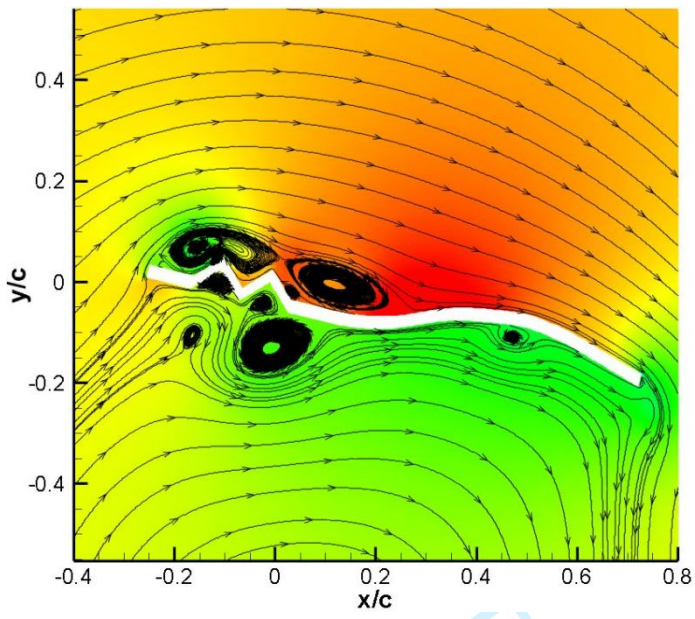

(b)
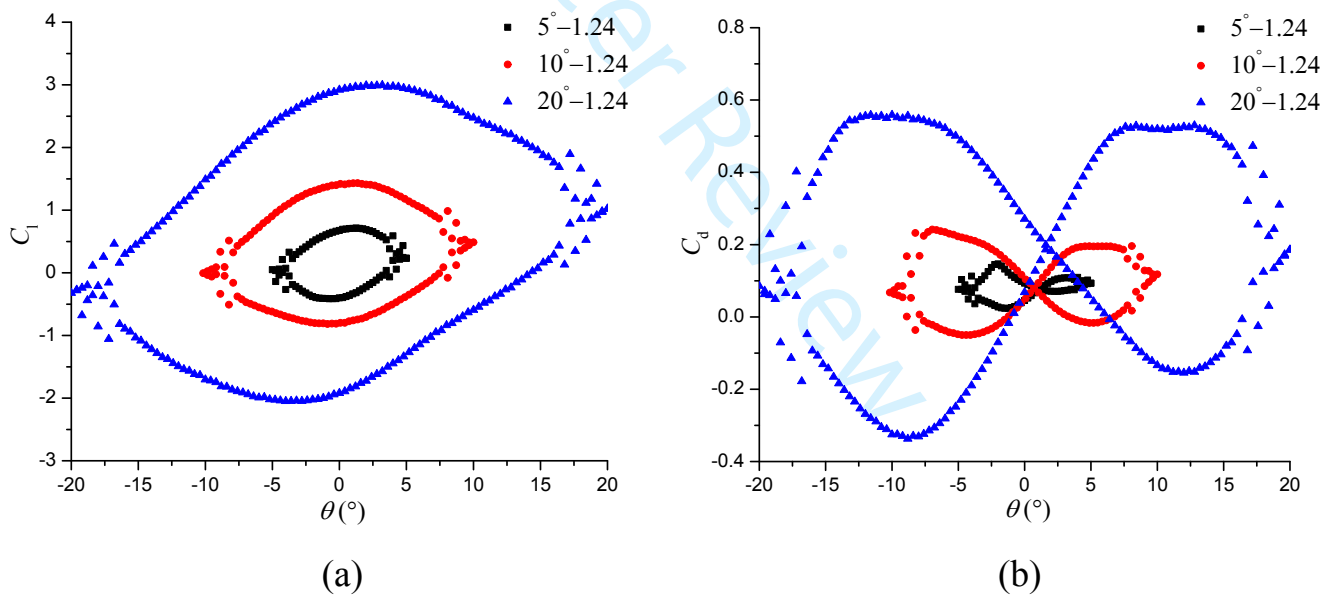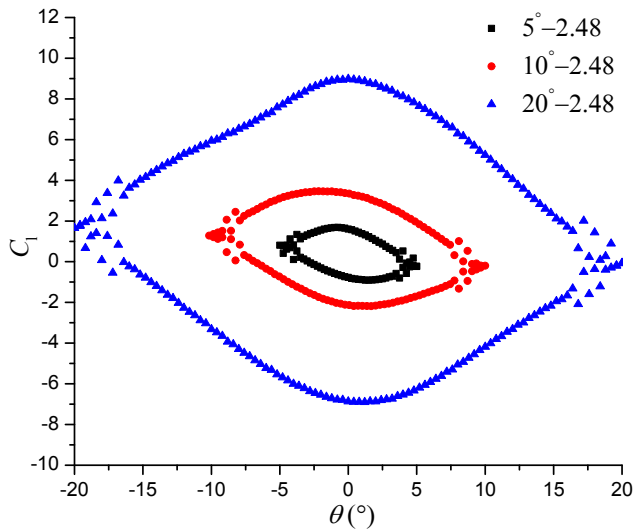
(c)
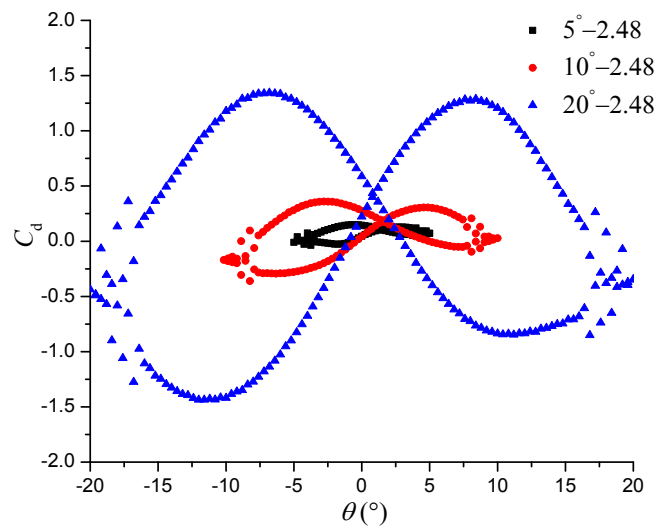
(d)
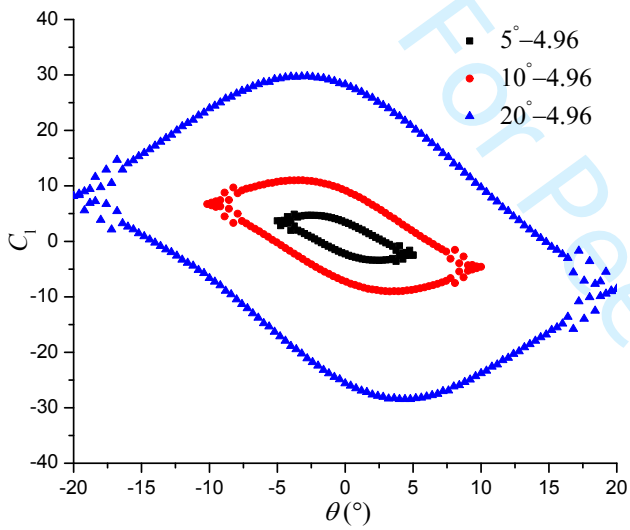
(e)

(f)

(g)

(h)

Fig.9 Instantaneous and time-averaged lift and drag coefficients. (a), (c) and (e) Instantaneous lift coefficients; (b), (d) and (f) Instantaneous drag coefficients; (g) Time-averaged lift coefficient; (h) Time-averaged drag coefficient.

17

1
2
3   The detailed flow structures over the hydrofoil surface are shown in figure 10
4   using the pressure distributions with the relative streamlines. The tested case is
5   hydrofoil A with thickness of 2mm, pitching amplitude of $20°$ and reduced
6   frequency of 2.48. Eight instants in a revolution are analyzed. From $t=T/8$ to $3T/8$,
7   over the upper surface, different vortices integrate into a large-scale structure above
8   the protrusions which convects downstream during the pitch-down process. At the
9   same time, the flow starts to separate near the leading edge on the lower surface. It
10 is obvious that a large fraction of the hydrofoil upper surface is occupied by the
11 high pressure, especially after the second protrusion. The low pressure on the lower
12 surface is also observed, resulting in the negative lift generation, especially at $t=T/4$
13 when the hydrofoil has the maximal negative lift coefficient. Then, at next time
14 $t=T/2$, as the hydrofoil has the maximal negative incidence, the high pressure exists
15 on a large part of the lower surface with smooth curvature and there is a
16 low-pressure region near the leading edge due to the flow separation, leading to the
17 lift coefficient reaching to the zero. Afterwards, the hydrofoil has the pitch-up
18 motion from $t=5T/8$ to T. The main feature is that the high pressure on the lower
19 surface gradually moves towards the leading edge, bringing about the gradual
20 increase of the lift coefficient. At $t=3T/4$, the hydrofoil has the maximal positive lift
21 coefficient. Moreover, when the hydrofoil incidence still increases from $t=7T/8$ to
22 T, the high level of the pressure on the lower surface decreases while the pressure
23 on the upper surface increases slowly. Additionally, a vortex is detected on the
24 lower surface with smooth curvature near the trailing edge during the pitch-up
25 motion, as a result of the shear layer flow separation. In a conclusion, it can be seen
26 that the main contributor to the lift change is the pressure distribution on the surface
27 with smooth curvature, which changes significantly with the prescribed oscillating
28 motion.

$p/(0.5*\rho*U_0^2)$

-11.1   -10.0   -8.89   -7.78   -6.67   -5.56   -4.45   -3.34   -2.23   -1.12   -0.01   1.10   2.21   3.32
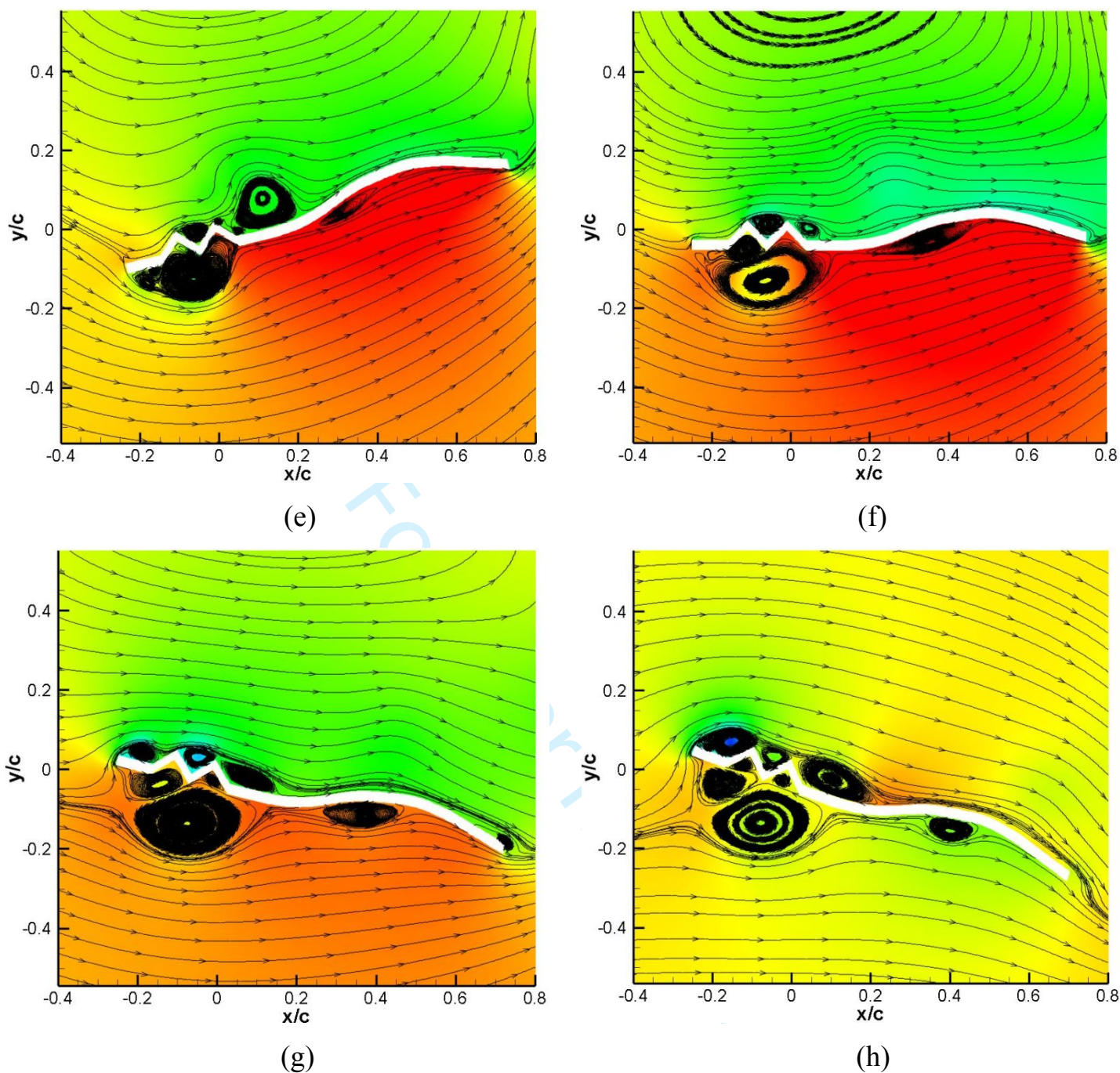
18

(a)

(b)

(c)

(d)
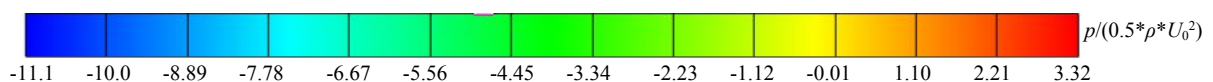
Fig.10 Instantaneous pressure distributions at different instants. (a) $T/8$; (b) $T/4$; (c) $3T/8$; (d) $T/2$; (e) $5T/8$; (f) $3T/4$; (g) $7T/8$; (h) T.

Figure 11 shows the instantaneous spanwise vorticity distribution at different k_{red} as the hydrofoil has the maximal positive incidence. According to the previous investigations, increasing k_{red} leads to the delayed flow structure. For an instance, an individual vortex, induced by the flow separation near the leading edge, is still visible over the lower surface. However, it has almost already disappeared at $k_{red}=1.24$ while it is still clear with high level of the positive vorticity at $k_{red}=4.96$. The vortex system is quite clear when the reduced frequency is 4.96, both on the hydrofoil surface and in the wake region. What is more, it is found that the vortex

20

shedding in the wake region is extremely different for various k_{red}. With the increase of k_{red}, the trajectory of the vortex street deflects downward and the distance of two adjacent vortex structures become short, which is possibly responsible for the change of the time-averaged lift and drag coefficients in figure 8g and 8h. Besides, the deflected wakes have great benefits to the production of the thrust. Hosseinjani and Ashrafizadeh [21] explained that the asymmetrical reverse Kármán vortex street can generate the side force, but its physics is still not understood well.
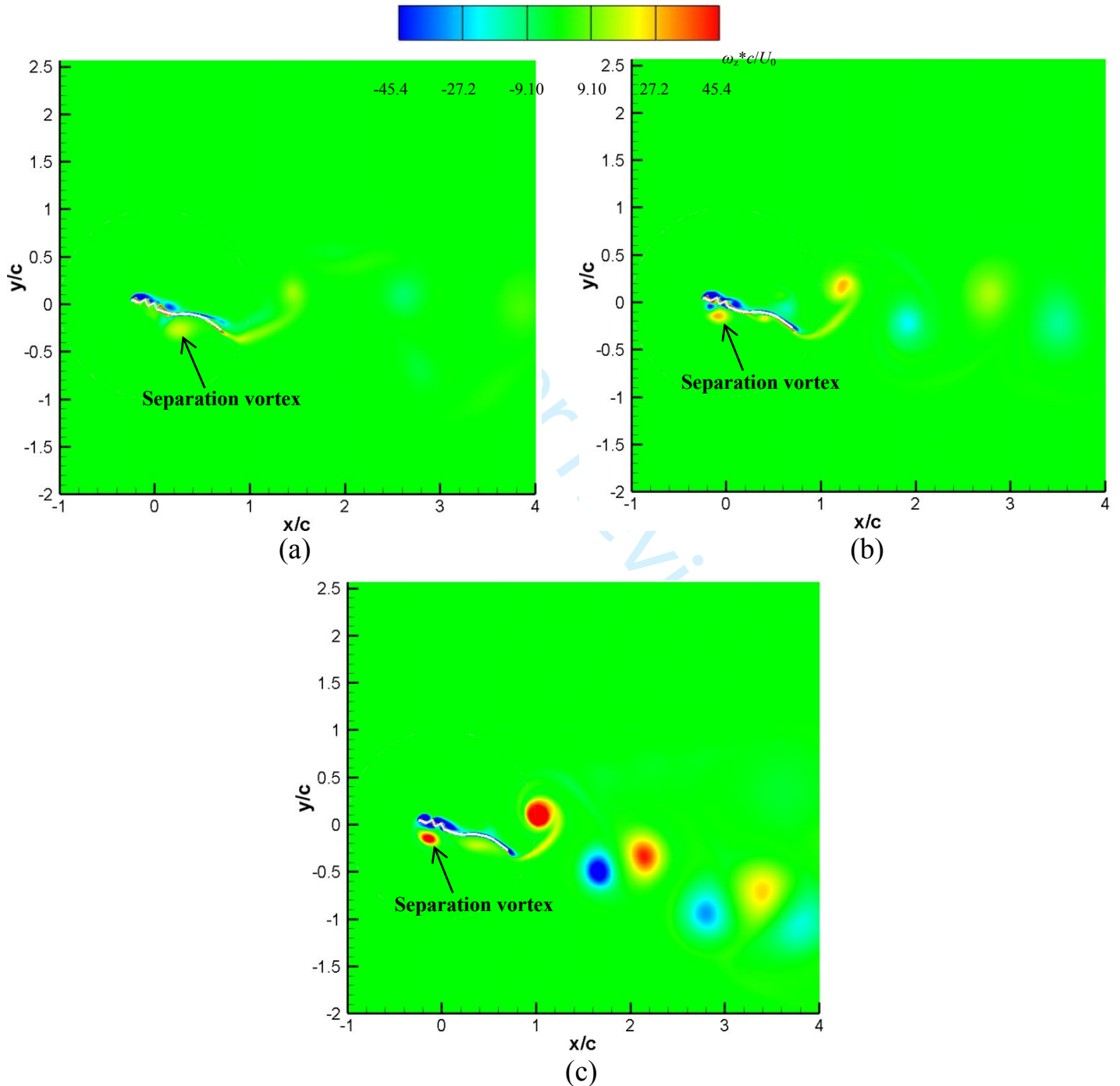
Fig.11 Spanwise vorticity at different k_{red}. (a) 1.24; (b) 2.48; (c) 4.96.

4.4 Effect of the Reynolds number

21

Reynolds number is also an important parameter to affect the performance and vortex evolution of the oscillating foils. The other three Reynolds numbers, including $Re=7\times10^3$, 2.8×10^4 and 5.6×10^4, are also tested in this study. The instantaneous and time-averaged lift and drag coefficients under different Reynolds number conditions at $k_{red}=2.48$ are plotted in figure 12. The maximal pitching angle is $10°$. It seems that the influence of the Reynolds number on the instantaneous lift variation is very weak generally, but there still has some difference at different stages. For instances, from the angle-of-attack of $0°$ to $-10°$ in the downstroke process, the high Reynolds number $Re=5.6\times10^4$ achieves the low negative lift coefficient, while from the incidence of $-10°$ to $0°$ in the upstroke process, the higher lift coefficient is evident at $Re=5.6\times10^4$. Then, when the incidence increases from $0°$ to $10°$, the lower lift coefficient at $Re=7\times10^3$ is more evident, which is the main reason why the mean lift coefficient increases with Re, as presented in figure 12c. Besides, the drag coefficient shown in figure 12b has the opposite trend compared with the change of the lift coefficient, especially from pitching angle of $5°$ to $10°$, where it has a relatively large discrepancy at various Re. As a consequence, the time-averaged drag coefficient in figure 12c decreases with Re.

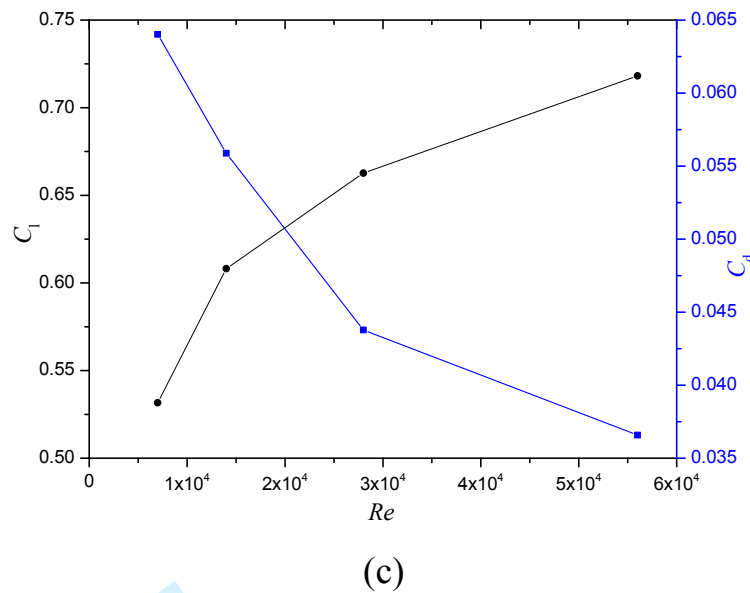(a)   (b)

(c)
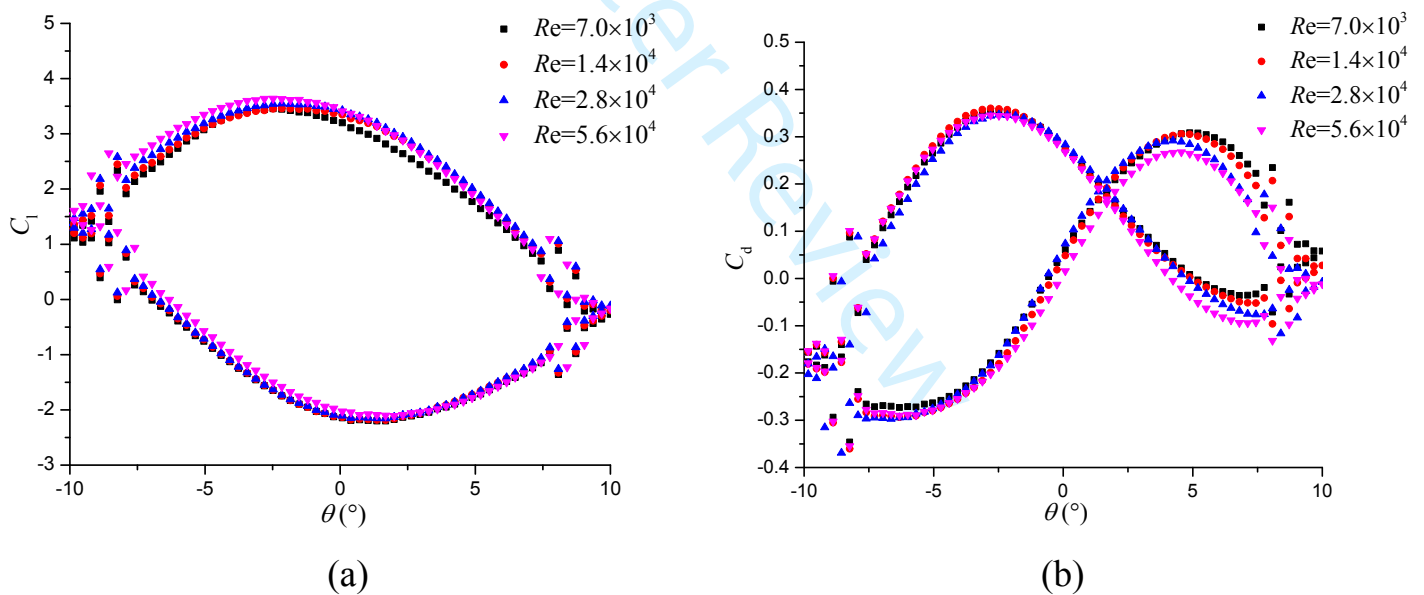
Fig.12 Performance curves at various Re. (a) Instantaneous lift coefficients; (b) Instantaneous drag coefficients; (c) Time-averaged lift and drag coefficients.

To investigate the difference of the lift coefficient at different Re, the pressure distributions along the hydrofoil surface at three instants are plotted in figure 13, when the pitching hydrofoil has the reduced frequency of 2.48 and maximal pitching amplitude of $10°$. At $t=3T/8$, the hydrofoil undergoes the downstroke process, and it has the negative incidence. It seems that the pressure difference between the upper and lower sides is relatively small, leading to the lower lift coefficient shown in figure 12a. The main difference is on the upper surface ranging from $x=0.2c$ to $0.5c$, where the pressure decreases with the increase of Re, especially at $Re=5.6×10^4$. Then, at next instant $t=5T/8$, the pressure difference for different Re is mainly at $x=0.3c\sim0.6c$ on the upper surface, and the largest magnitude is obtained by $Re=5.6×10^4$. Finally, at $t=13T/16$ in the upstroke motion, both the upper and lower surfaces have different pressure distributions for different Re, which is mainly at $x=0.4c\sim0.8c$ on the upper surface and at $x=0.6c\sim1.0c$ on the lower surface. Obviously, the Reynolds number of $7×10^3$ achieves the lowest lift coefficient as a result of the small pressure difference. In general, it is observed that the Reynolds number has some influence on the pressure distribution on the surface with smooth curvature at different stages, leading to the change of the lift coefficient of the oscillating hydrofoil.
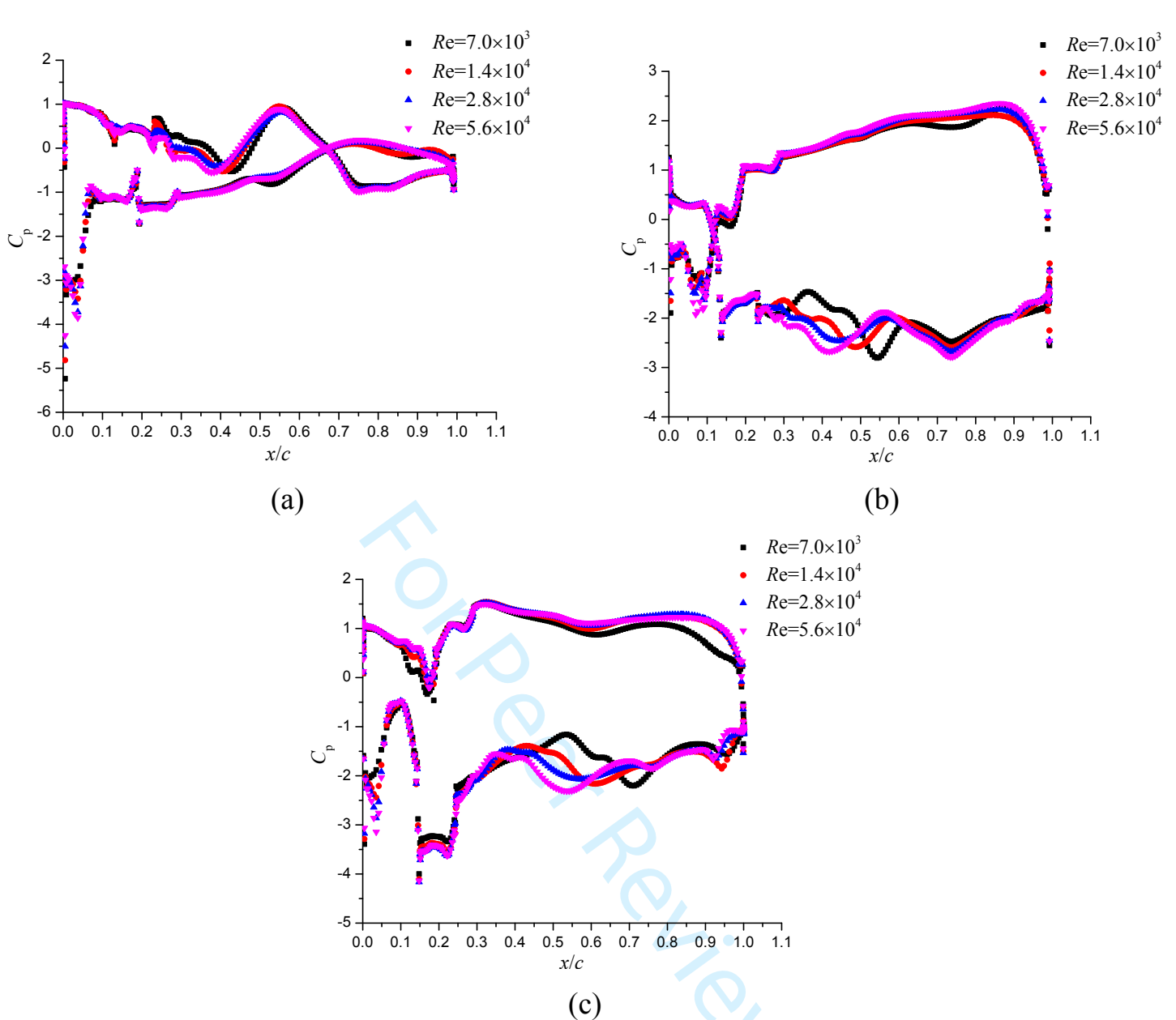
(a)

(b)

(c)

Fig.13 Pressure distributions at different instants. (a) $3T/8$; (b) $5T/8$; (c) $13T/16$.

The wake patterns, presented by the spanwise vorticity, are shown in figure 14 at different Re. The instant adopted here is when the hydrofoil has the maximal pitching angle of $10°$. The wake flows under different Re conditions have different exhibitions. At $Re=7\times10^3$ and 1.4×10^4, the flow shows the same pattern, but the distance of the adjacent vortex structure is different, which is both affected by the low freestream velocity and hydrofoil pitching frequency. When the Reynolds number increases to 2.8×10^4 and 5.6×10^4, there is almost no difference in vortex structure in the wake region, but the flow pattern differs from that at $Re=7\times10^3$ and 1.4×10^4. Therefore, it shows that the Reynolds number still has the effect on the wake morphology, especially at low Reynolds number.
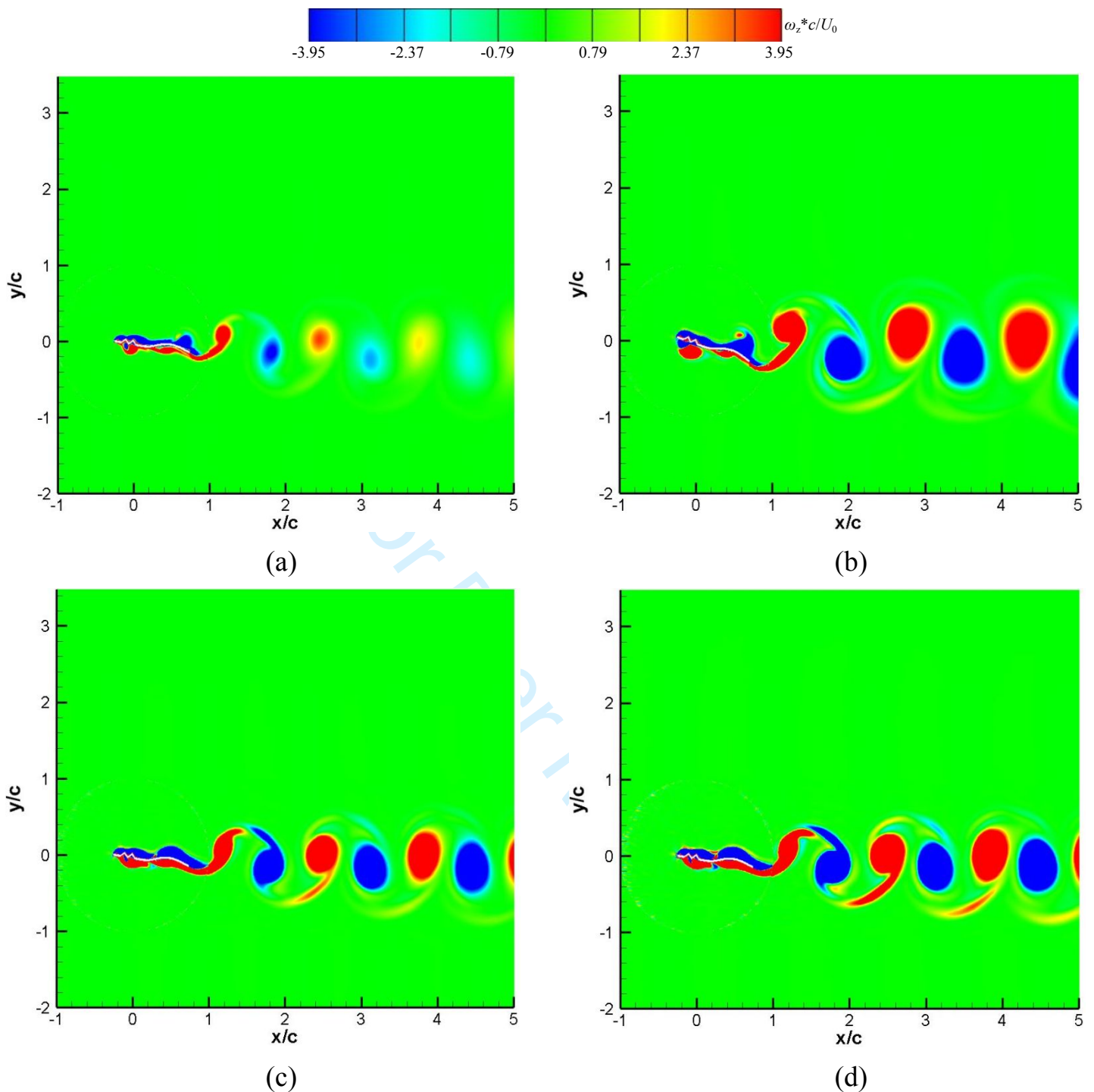
24

Fig.14 Wake morphology at different Re. (a) 7×10^3; (b) 1.4×10^4; (c) 2.8×10^4; (d) 5.6×10^4.

4.5 Effect of the hydrofoil geometry

Two hydrofoils with different geometries shown in figure 2a and 2b are investigate in this part, to study the vortex structure over the hydrofoil surface and in the wake region, at different k_{red}. The maximal pitching amplitude is 10°. The instantaneous and time-averaged lift and drag coefficients of two hydrofoils are plotted in figure 15. At k_{red}=1.24, within a certain range, for example, from +5° to -5° in the downstroke, hydrofoil B generates the larger negative lift coefficient than

25

hydrofoil A. Then, the positive lift coefficient obtained by hydrofoil A is larger than that of hydrofoil B, in the range of -10°~0° as it has the pitch-up motion. As a result, the mean lift coefficient of hydrofoil A at this reduced frequency is larger than that produced by hydrofoil B, as shown in figure 15g. However, at k_{red}=2.48 and 4.96, hydrofoil A can obtain the higher lift coefficient in the whole rotating cycle, especially at k_{red}=2.48. The drag coefficient is quite complicated and different for two hydrofoils, which is closely associated with the wakes. But it is observed that the drag coefficients obtained by those two hydrofoils show the opposite trend. For a specific example, at k_{red}=2.48, the variation of the drag coefficient of hydrofoil A at incidences which are smaller than 0° is similar with that of hydrofoil B at incidences larger than 0°, which nearly appears at all three k_{red}. Regarding the distributions of the mean lift and drag coefficients, it is observed that the lift coefficient produced by hydrofoil A is much higher than that of hydrofoil B, which is more obvious with the increase of k_{red}. Moreover, the drag coefficient decreases significantly with k_{red} for both two hydrofoils. At high reduced frequency of 4.96, the drag has the negative value and it becomes the thrust, which is larger for hydrofoil B.
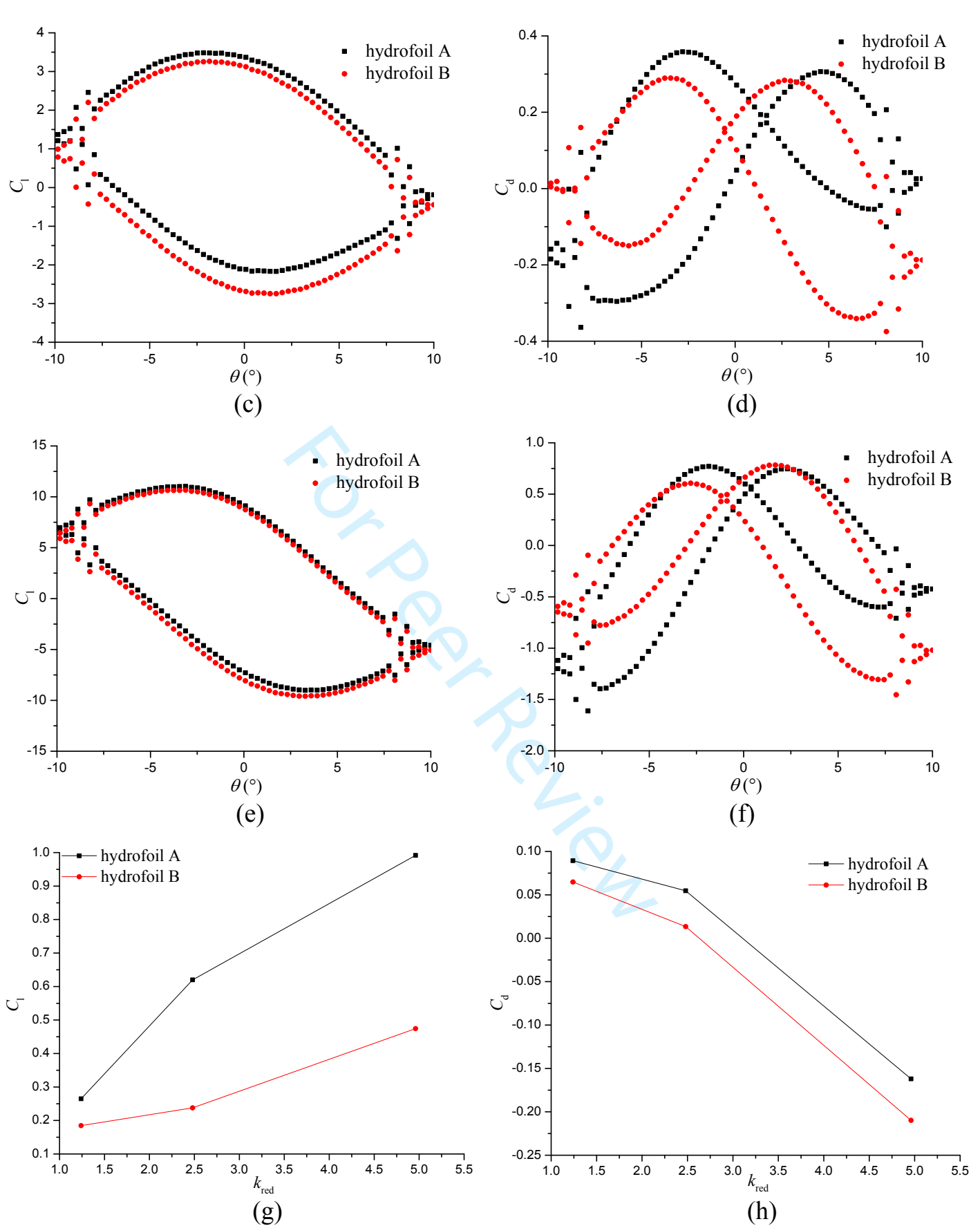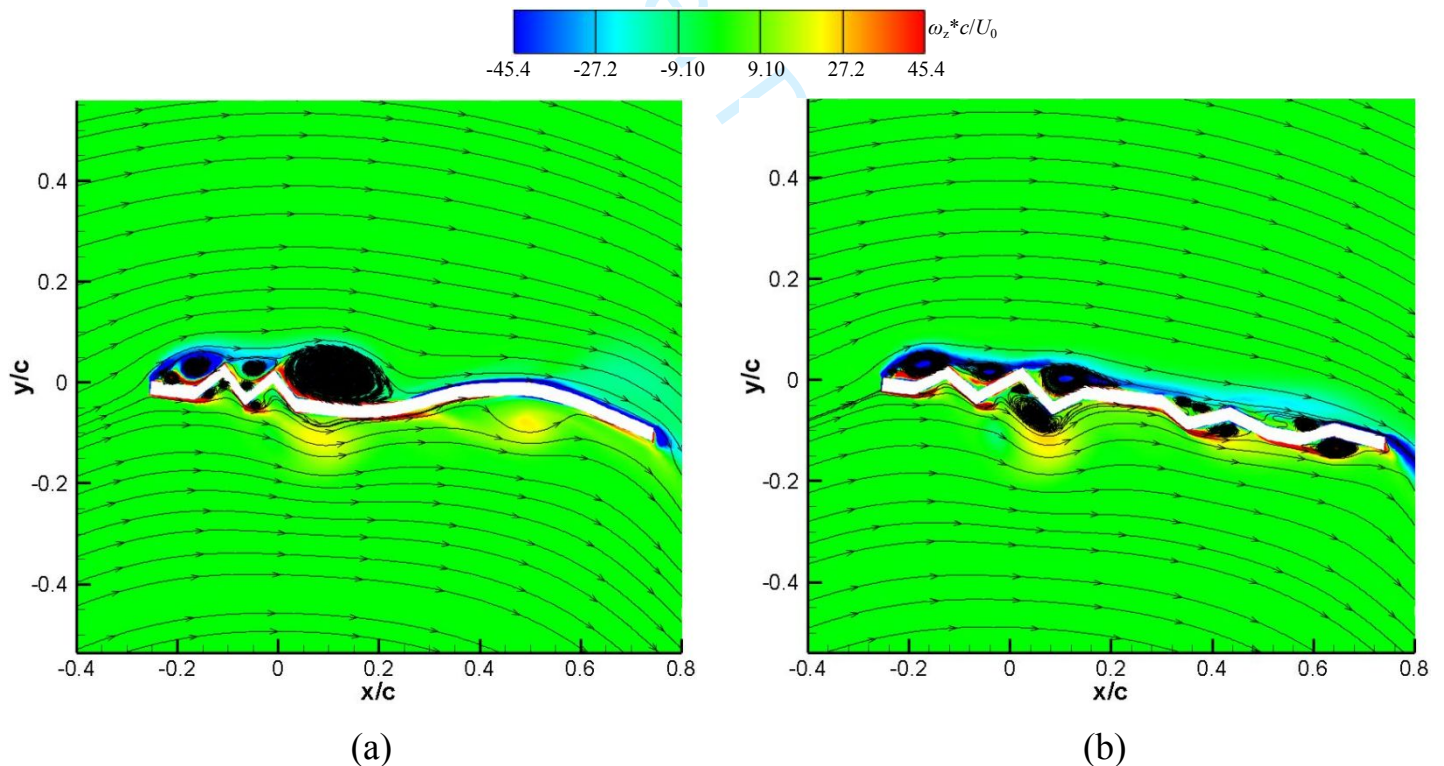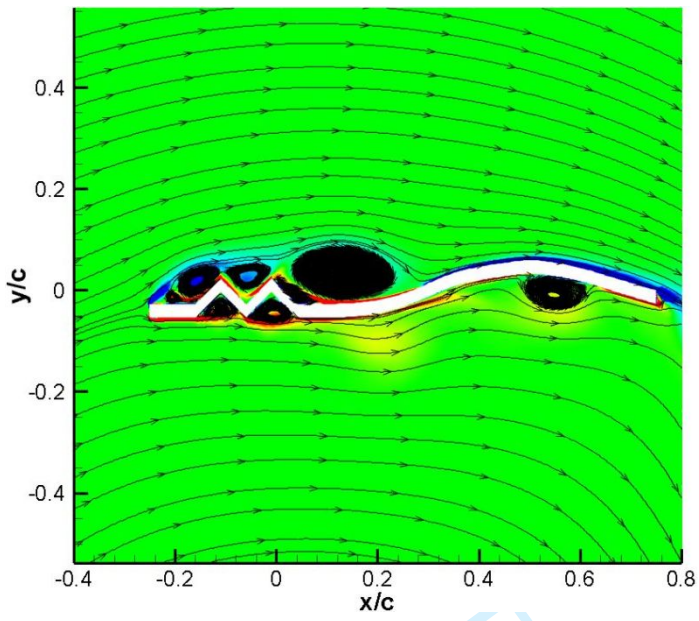

(a)

(b)
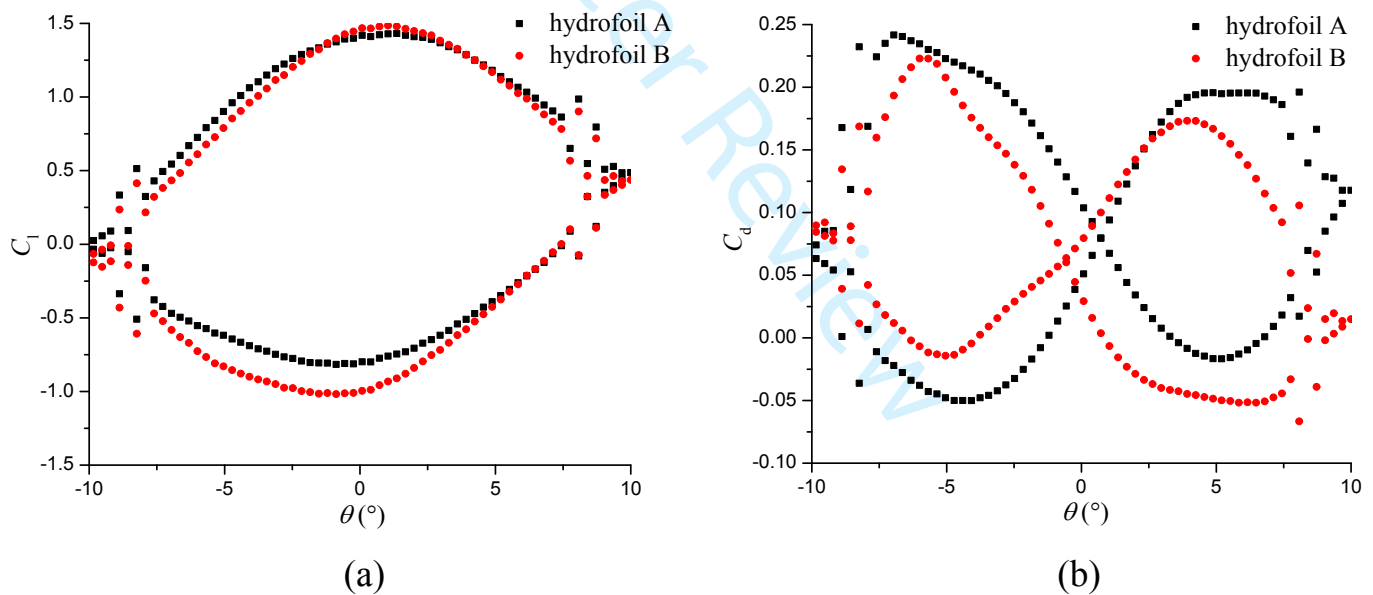
Fig.15 Instantaneous and time-averaged lift and drag coefficients for two hydrofoils at different k_{red}. (a) and (b) 1.24; (c) and (d) 2.48; (e) and (f) 4.96; (g) Mean lift coefficient; (h) Mean drag coefficient.
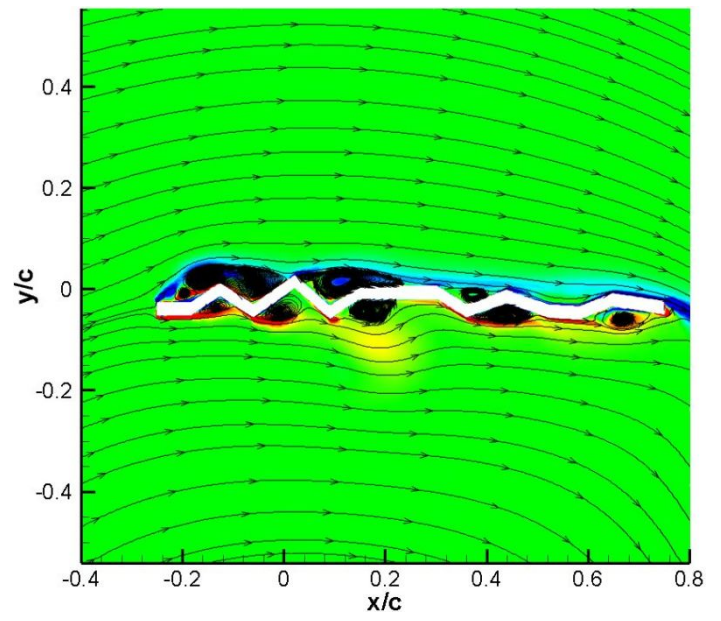
27

The detailed flow structures at k_{red}=2.48 are shown in figure 16, for two different hydrofoils, using the spanwise vorticity contours coupled with streamlines. The maximal pitching amplitude is 10°. Over the hydrofoil A and B, there are a plenty of vortices with different scales, depending on the geometry with different corrugations. From t=T/8 to 3T/8, the hydrofoil experiences the pitch-down motion, the trapped vortices on the upper surface moves downward and integrate into a large-scale structure. Similarly, more vortices are generated over the lower surface which migrate towards the trailing edge due to the oscillation, leading to the vortices attached on the trailing edge shedding into the wakes. Besides, it is observed that the discontinuous shear layer on the protrusions becomes continuous gradually and develops downward, especially on the lower surface. Afterwards, in the upstroke process from t=5T/8 to 7T/8, the discrete vortices on the lower surface become a large vortex while more vortex emerge over the upper surface near the leading edge. At the same time, the boundary layer with high positive vorticity on the lower surface near the trailing edge also sheds into the wakes. It seems that the vortex system of hydrofoil B is more complicated than hydrofoil A, determined by the large number of corrugations, which can result in the massive flow separation and more trapped vortices.
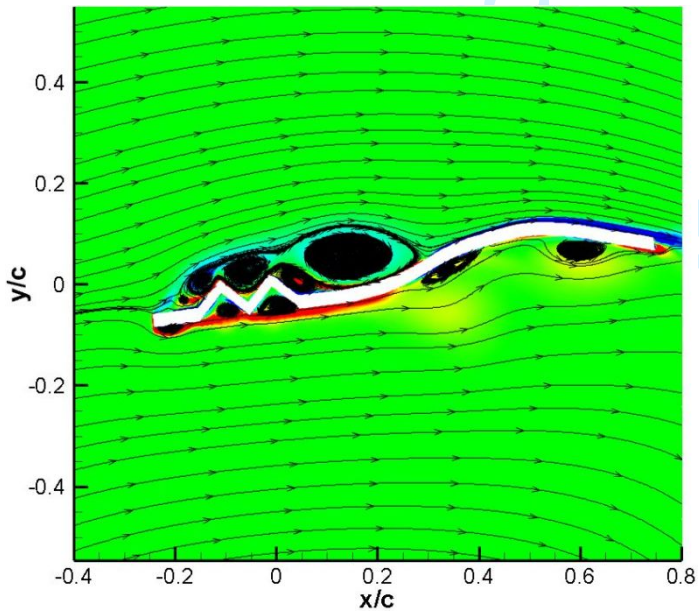

(a)   (b)

(c)

(d)

(e)

(f)

29

Journal name

(g)

(h)

(i)

(j)

(k)   (l)

Fig.16 Distributions of vorticity contours with streamlines at different instants. The left column is hydrofoil A and the right column is hydrofoil B. (a) and (b) $T/8$; (c) and (d) $T/4$; (e) and (f) $3T/8$; (g) and (h) $5T/8$; (i) and (j) $3T/4$; (k) and (l) $7T/8$.

Following the vortical flows in figure 16, the pressure coefficients of two hydrofoils at the same instant are plotted in figure 17, to study the effect of vortex evolution on the lift coefficient. As shown in figure 17, the pressure distributions for hydrofoil A and B show some difference, depending on the instant when the high pressure occurs. At instants $t=T/8$, $T/4$ and $3T/8$, the high pressure is on the aft part of hydrofoil A from $x/c=0.2$, shown in figure 10a, which results in the evident pressure difference compared with hydrofoil B. However, when the hydrofoil has the upstroke motion from $t=5T/8$ to $7T/8$, the high pressure emerges on the lower surface, which makes the obvious pressure difference between hydrofoil A and B. In brief, the pressure distribution of hydrofoil B is relatively flat due to the more corrugations. The main pressure difference is on the smooth surface of hydrofoil A where the high pressure occurs depending on the state of the oscillating motion.
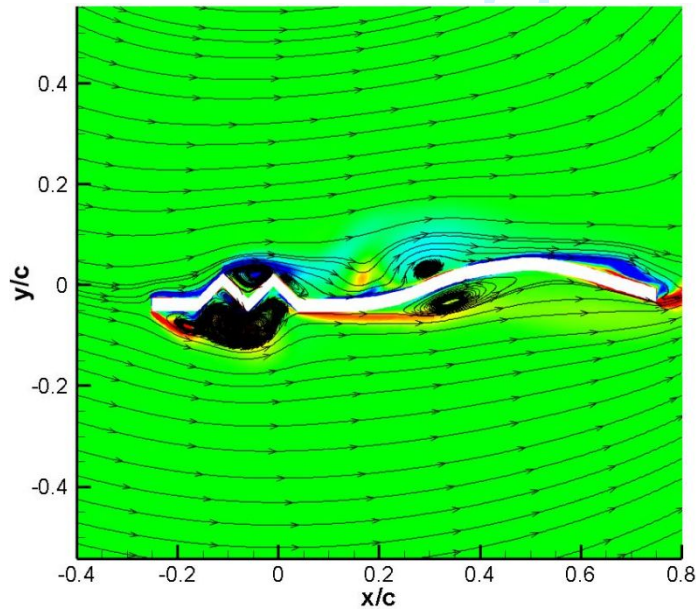
31

1
2
3
4
5
6
7
8
9
10
11
12
13
14
15
16
17
18
19
20
21
22
23
24
25
26
27
28
29
30
31
32
33
34
35
36
37
38
39
40
41
42
43
44
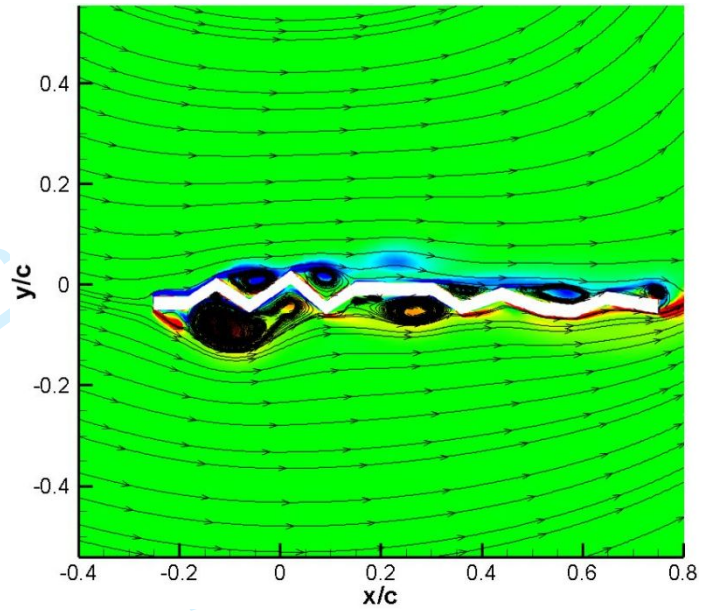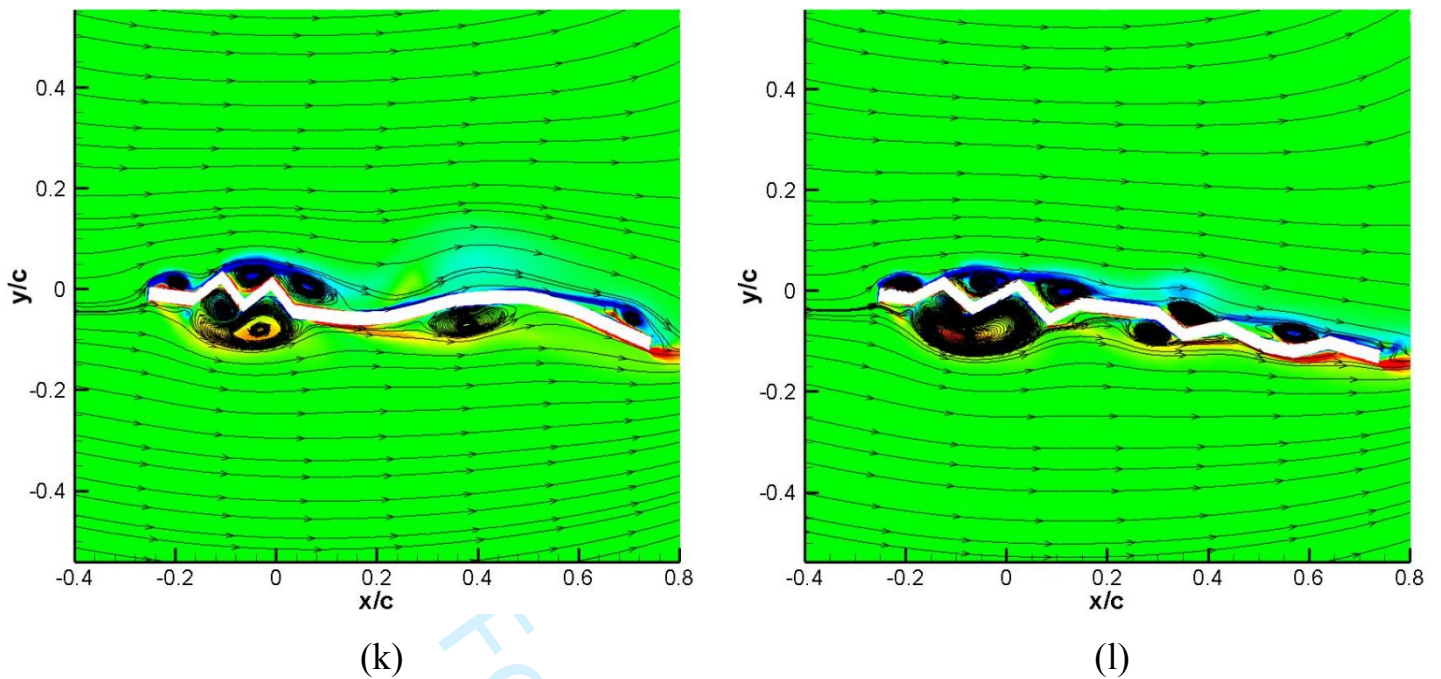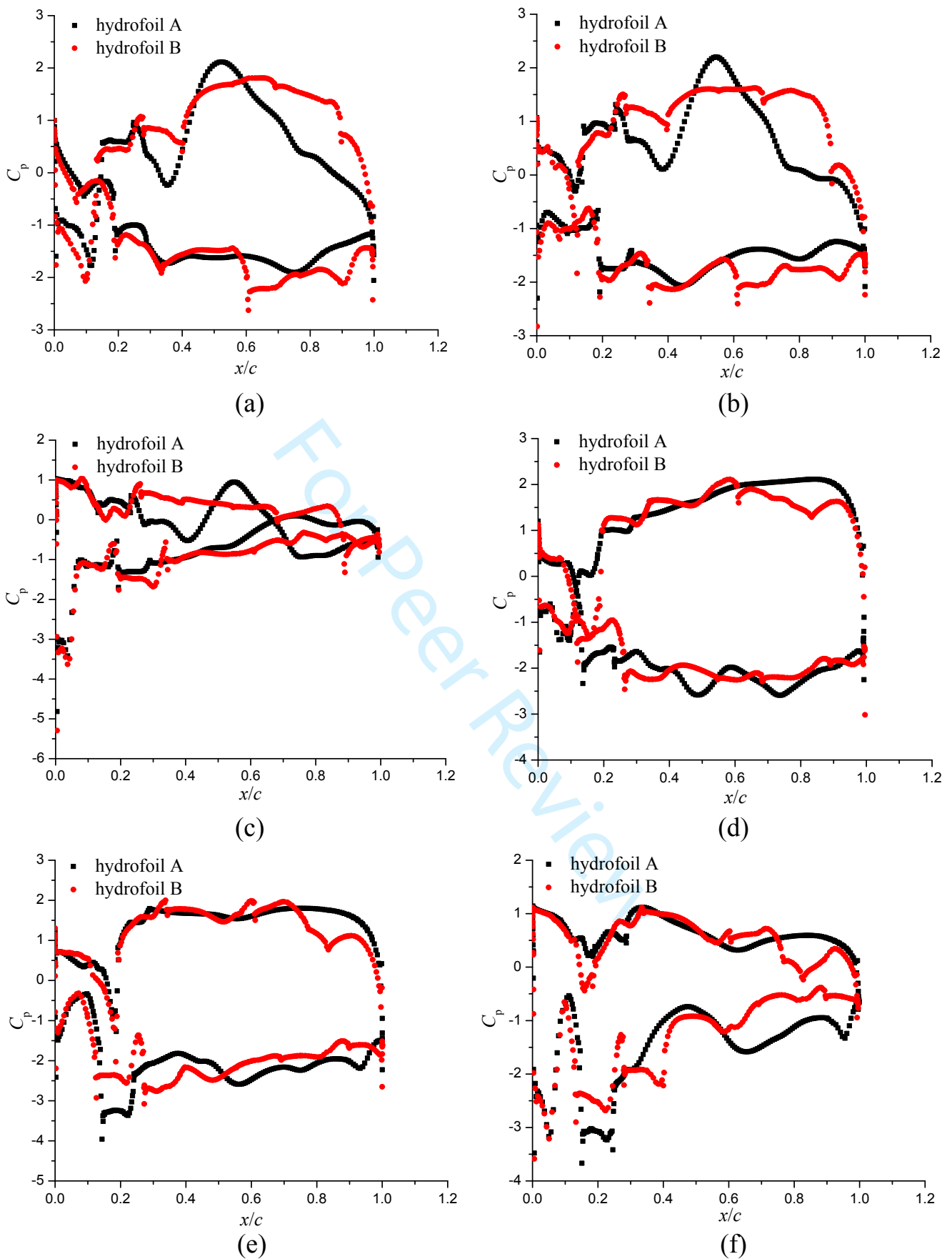45
46
47
48
49
50
51
52
53
54
55
56
57
58
59
60

Fig.17 Distributions of pressure coefficients for two hydrofoils at different instants. (a) $T/8$; (b) $T/4$; (c) $3T/8$; (d) $5T/8$; (e) $3T/4$; (f) $7T/8$.

32

The power spectra of the pressure at different locations for hydrofoil A and B are shown in figure 18. The primary frequency is about 2 Hz, which is the same with the pitching frequency of the hydrofoil. The corresponding Strouhal number, defined by $St=fA/U_0$ (A is the trailing edge pitching amplitude) is about 0.21, which is almost consistent with the frequency of the Von Karman vortex street. In figure 18a, the monitered point is located inside the first hollow near the leading edge and different frequency are detected. However, when it is located at the second and third hollow, the number of the high sub-frequency is decreased and the power of the sub-frequency is also reduced. Compared with hydrofoil A, the power of the high sub-frequency is much smaller for hydrofoil B, which is possibly induced by the relatively stable trapped vortices inside the hollows. When it comes to the wake flows, it shows that the power of the primary frequency gradually increases while it decreases for the secondary frequency. At $x/c=3.33$, they nearly have the same magnitude. Simultaneously, the effect of small scales is significantly weakened far away from the rotating part, which can be presented in figure 18f shown by the reduction of the high frequency energy. Therefore, it concludes that near the hydrofoil surface, the power of the high frequency has some difference for hydrofoil A and B, due to the development of trapped vortices as a consequence of the different hydrofoil shapes. In the wake region, the high frequency energy is reduced quickly far away from the rotating part due to the dissipation of the wake vortex flows. It is also observed that the distribution of the frequency is not associated with the hydrofoil shape, especially near the leading edge and in the wake region, which is more related to the pitching frequency.
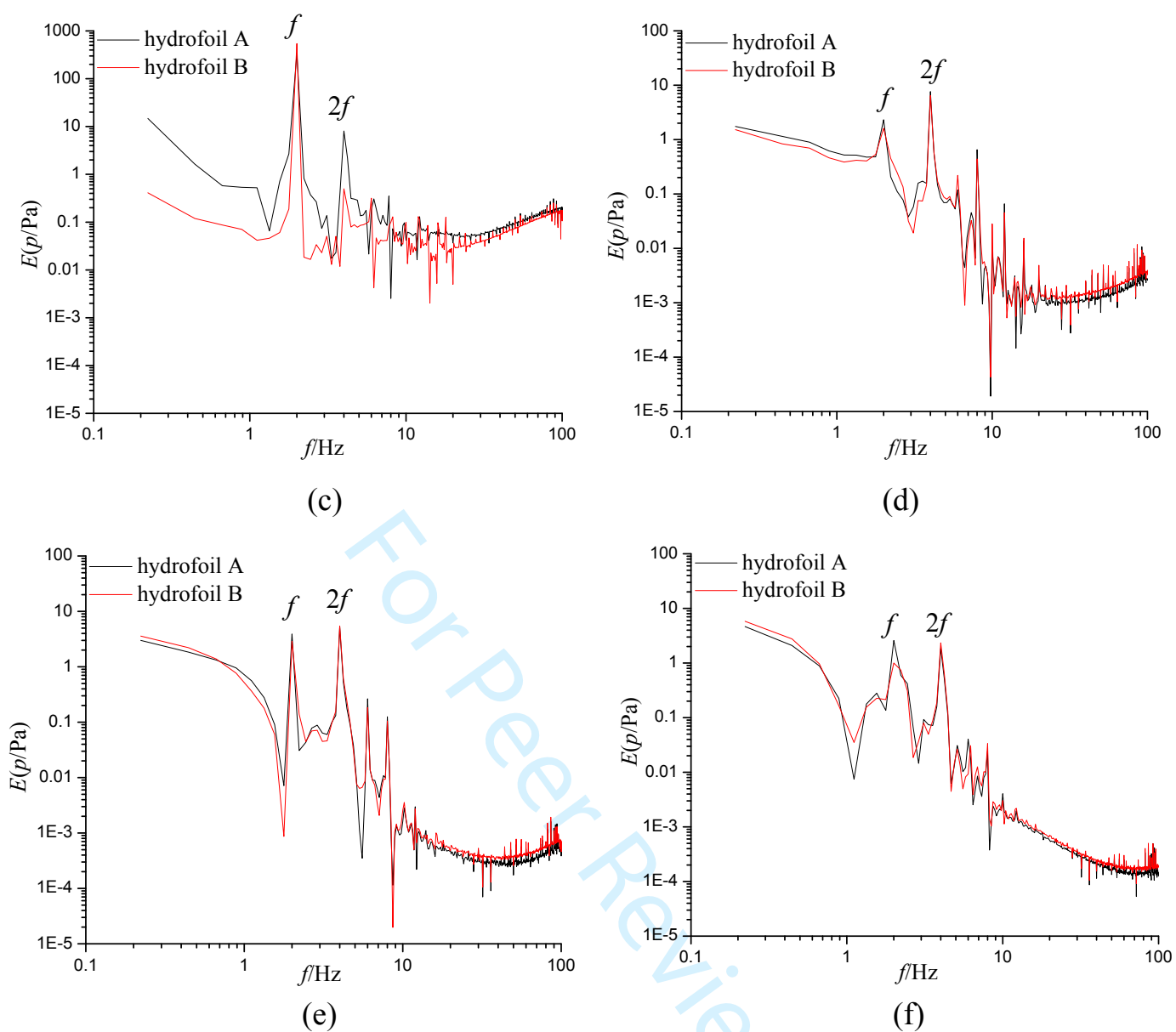

(a)

(b)
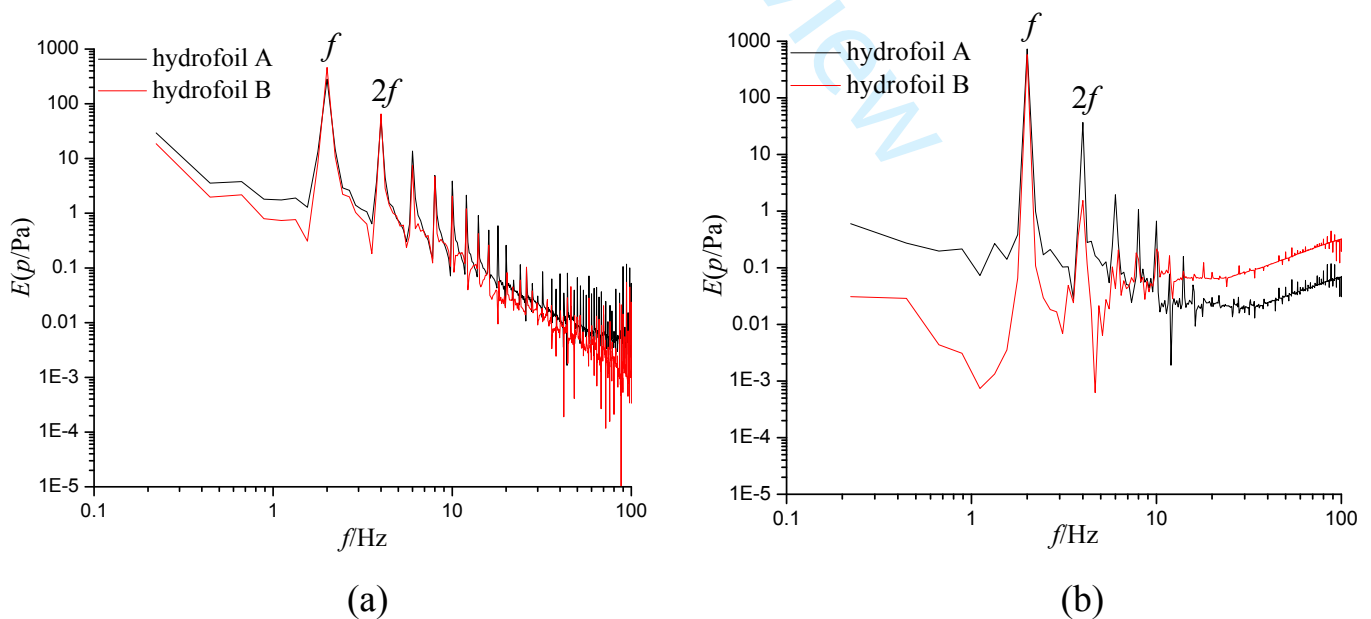
Fig.18 Power spectra analysis of the pressure for two hydrofoils at different locations. (a) In the first hollow on the upper surface; (b) In the second hollow on the upper surface; (c) In the third hollow on the upper surface; (d) x/c=1.33; (e) x/c=2; (f) x/c=3.33.

The mean streamwise velocity profiles in the wake region are plotted for two hydrofoils in figure 19. Evidently, the morphology of the mean wake flows varies significantly at different locations. In figure 19a and 19b, the wake flow totally exhibits the thrust-indicative profile, which indicates that the upper vortex row has the counterclockwise rotation while it has the clockwise rotation for the lower vortex. However, the hydrofoil B has the relatively large streamwise velocity peak compared with hydrofoil A. Then, it is observed that there is a transition from thrust-indicative to drag-indicative profile away from the trailing edge. By the comparison, it is found that the wake transition of hydrofoil A is more apparent, which should be responsible for the large variation of the predictive drag between
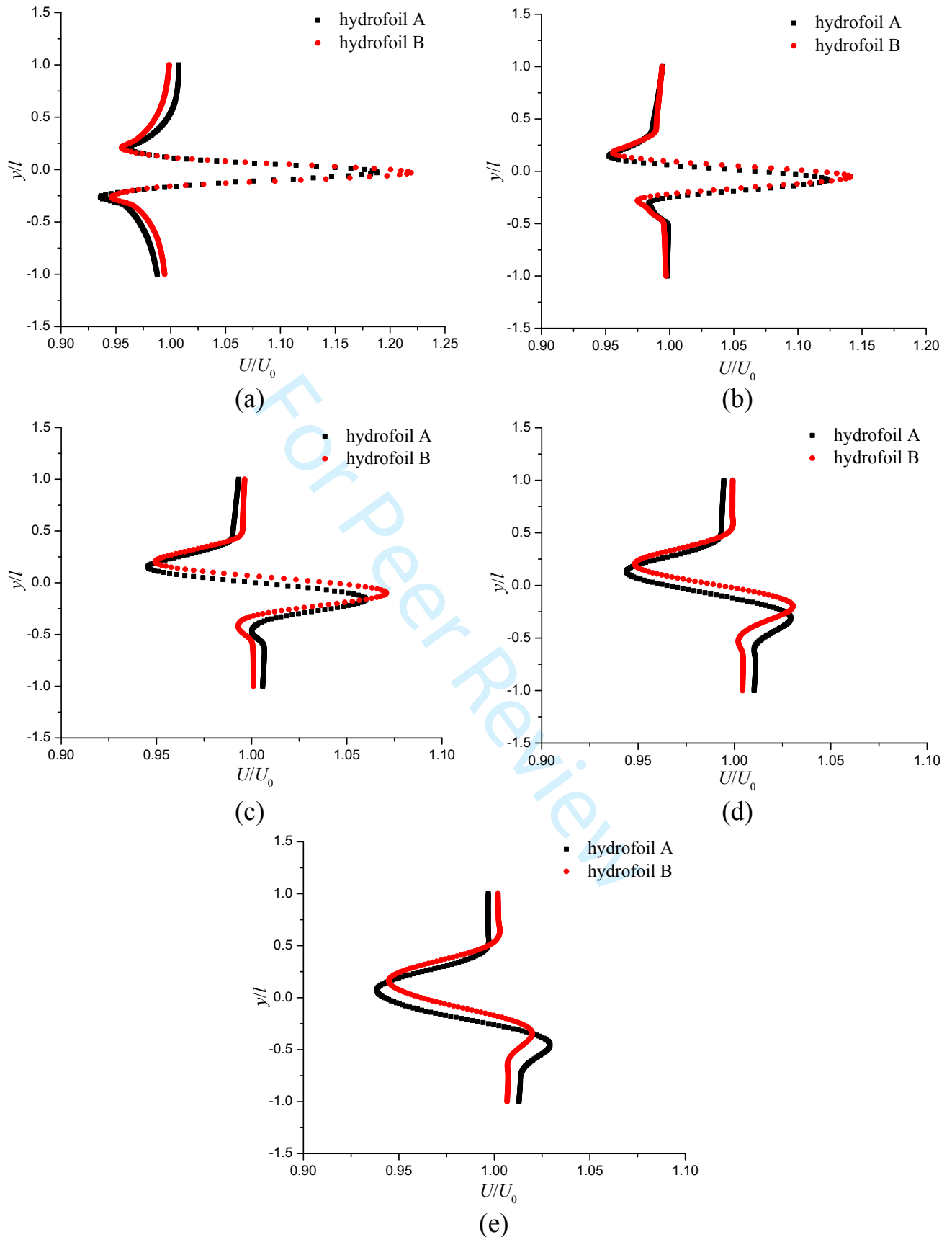
34

two hydrofoils shown in figure 15.

Fig.19 Velocity profiles in the wake region. (a) x/c=1.33; (b) x/c=2.67; (c) x/c=4; (d) x/c=5.33; (e) x/c=6.67.

35

4.5 Effect of the hydrofoil thickness

The hydrofoil A with the thickness of 2mm, 5mm and 8mm, is employed to study the thickness effect on the lift and drag coefficients, as well as the vortex evolution at k_{red}=2.48. The maximal pitching amplitude is 10°. According to the distributions of instantaneous lift and drag coefficients in a rotating cycle, it shows that with the increase of the hydrofoil thickness, the change of the lift coefficient is not obvious, compared with the drag coefficient. However, there is still some difference in instantaneous lift coefficient from +10° to 0°, -10° to -5° and 0° to +10°. In addition, the large part of the drag coefficient for the case with the thickness of 8mm is positive. Based on the figure 20c, it seems that both the lift and drag coefficients increases with the increase of the thickness, especially for the drag coefficient when the thickness increases from 5mm to 8mm. However, when it comes to the lift/drag ratio, it shows that the magnitude of this parameter decreases obviously as the thickness increases, which can give the inspiration to the designer for a better choice of the hydrofoil shape.
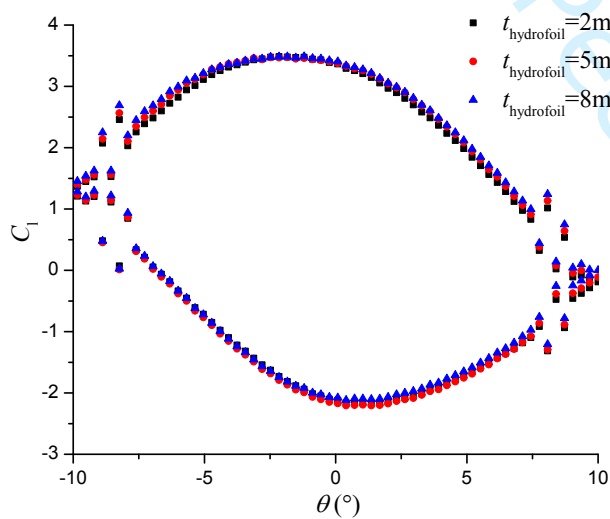
(a)
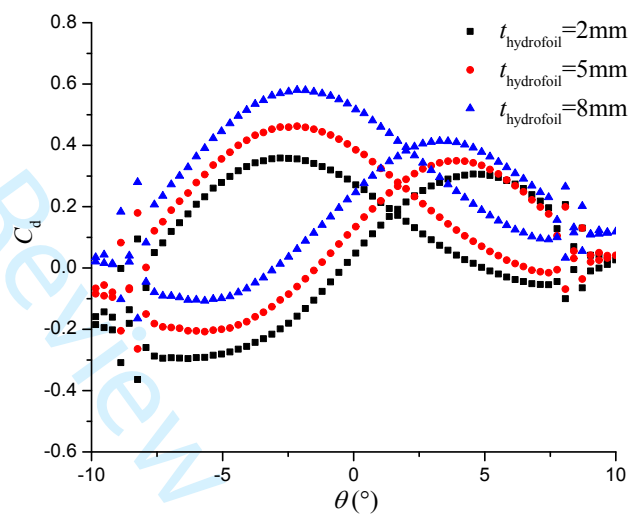
(b)
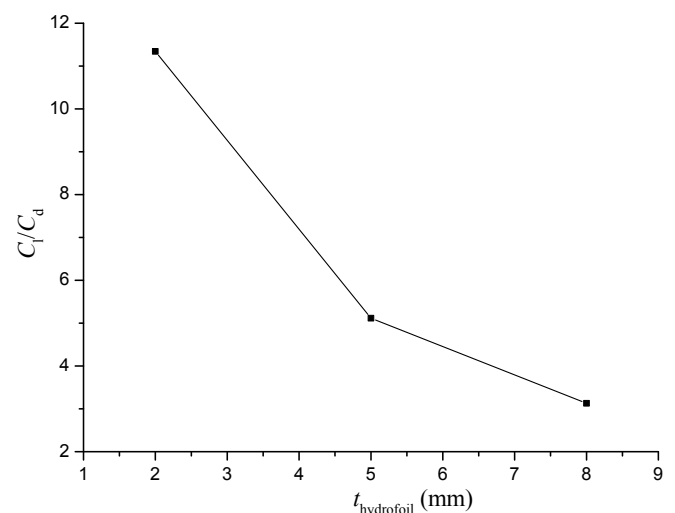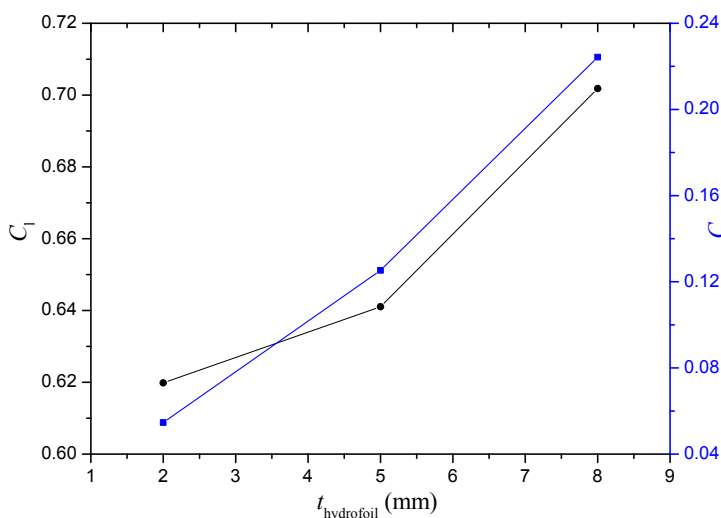
(c)   (d)

Fig.20 Performance of hydrofoil A with different thickness. (a) Instantaneous lift coefficient; (b) Instantaneous drag coefficient; (c) Mean lift and drag coefficients.

To reveal the lift difference for the hydrofoil with different thicknesses, the flow structures at an instant when the hydrofoil has the incidence of -7.5°, are presented in figure 21, using the spanwise vorticity contours and pressure distributions. In the upstroke process, there is the flow separation near the leading edge on the lower surface and the pressure has large difference for three hydrofoils. But after x/c=0.2, the pressure is almost unchanged. However, on the upper surface, the pressure distribution shows extremely different trend, especially after the second protrusion (x/c=0.2~0.45) where the induced vortex with high positive vorticity and large-scale separation vortex with negative vorticity coexist. Therefore, when the hydrofoil experiences the upstroke motion, the lift variation for different hydrofoils is mainly induced by the vortex evolution on the upper surface.

ω_z*c/U_0

-45.4   -27.2   -9.10   9.10   27.2   45.4
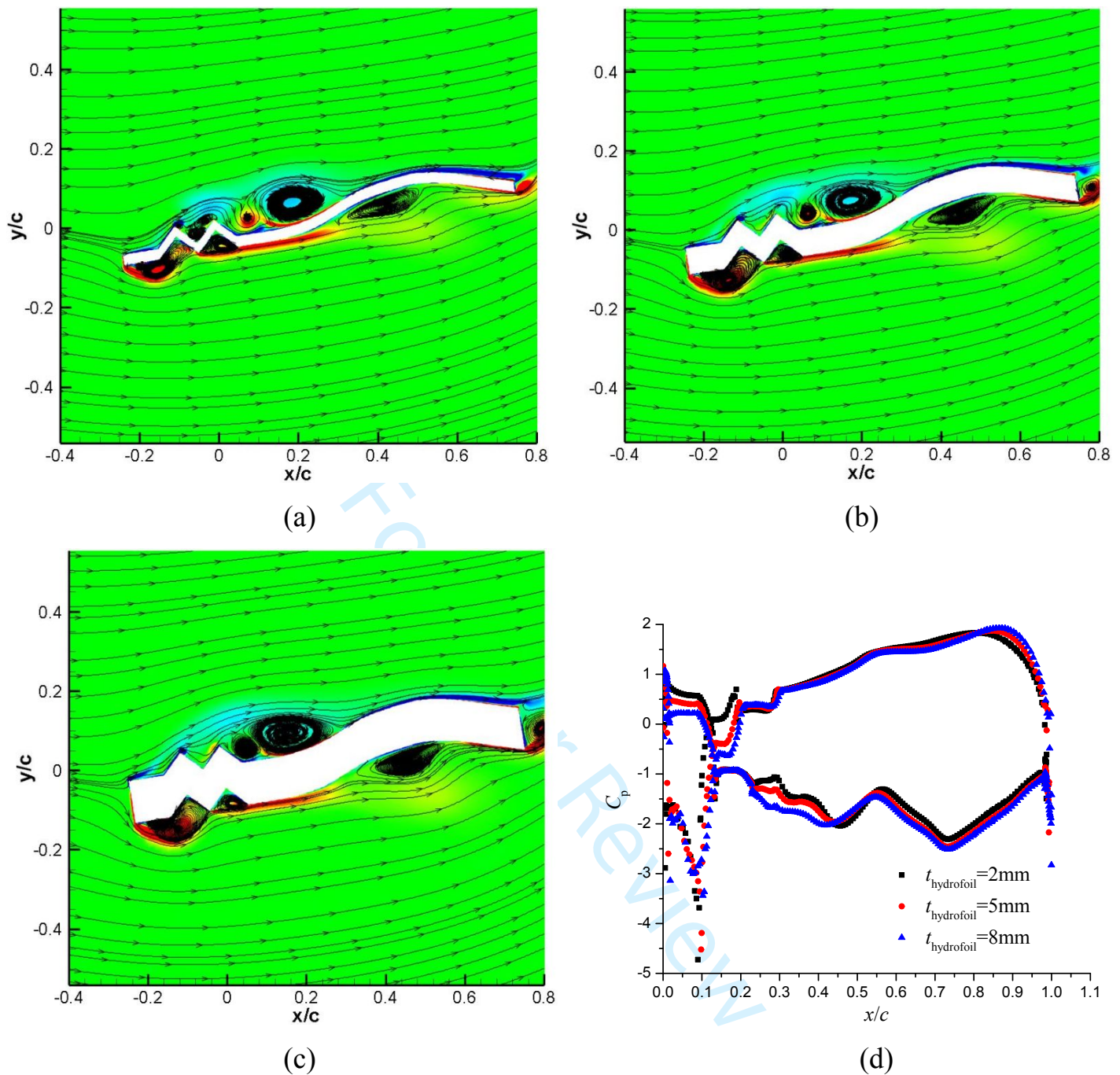
37

(a)

(b)

(c)

(d)
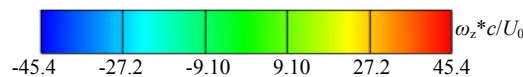
Fig.21 Flow structures and pressure distributions for hydrofoils with different thicknesses. (a) 2mm; (b) 5mm; (c) 8mm; (d) Pressure coefficients.

The gross feature of the wake flow characterized by the mean streamwise velocity profiles are shown in figure 22 at different locations. At x/c=1.33, the wake is shown as the thrust-indicative type, but the thin hydrofoil has the largest velocity peak. Then, at next position, both the thrust-indicative and drag-indicative wake profiles are detected, especially for the hydrofoil with the thickness of 8mm. Afterwards, the wake velocity profile has a transition from x/c=2.67 to 4, in which the hydrofoil with the largest thickness has already had the drag-indicative profile. Finally, at last two locations, the wake profile totally exhibits the drag-indicative

38

type, but the magnitude of the velocity peak is relatively small for the hydrofoil with the thickness of 2mm, which is closely associated with the drag coefficient distribution in figure 20.
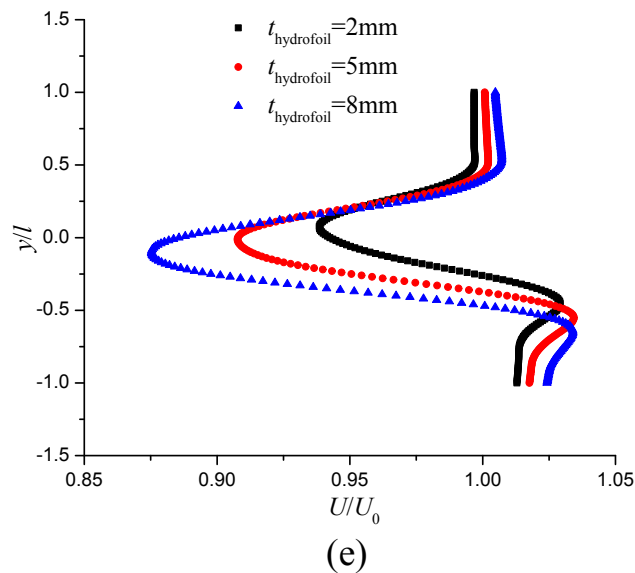

(a)

(b)

(c)

(d)

(e)
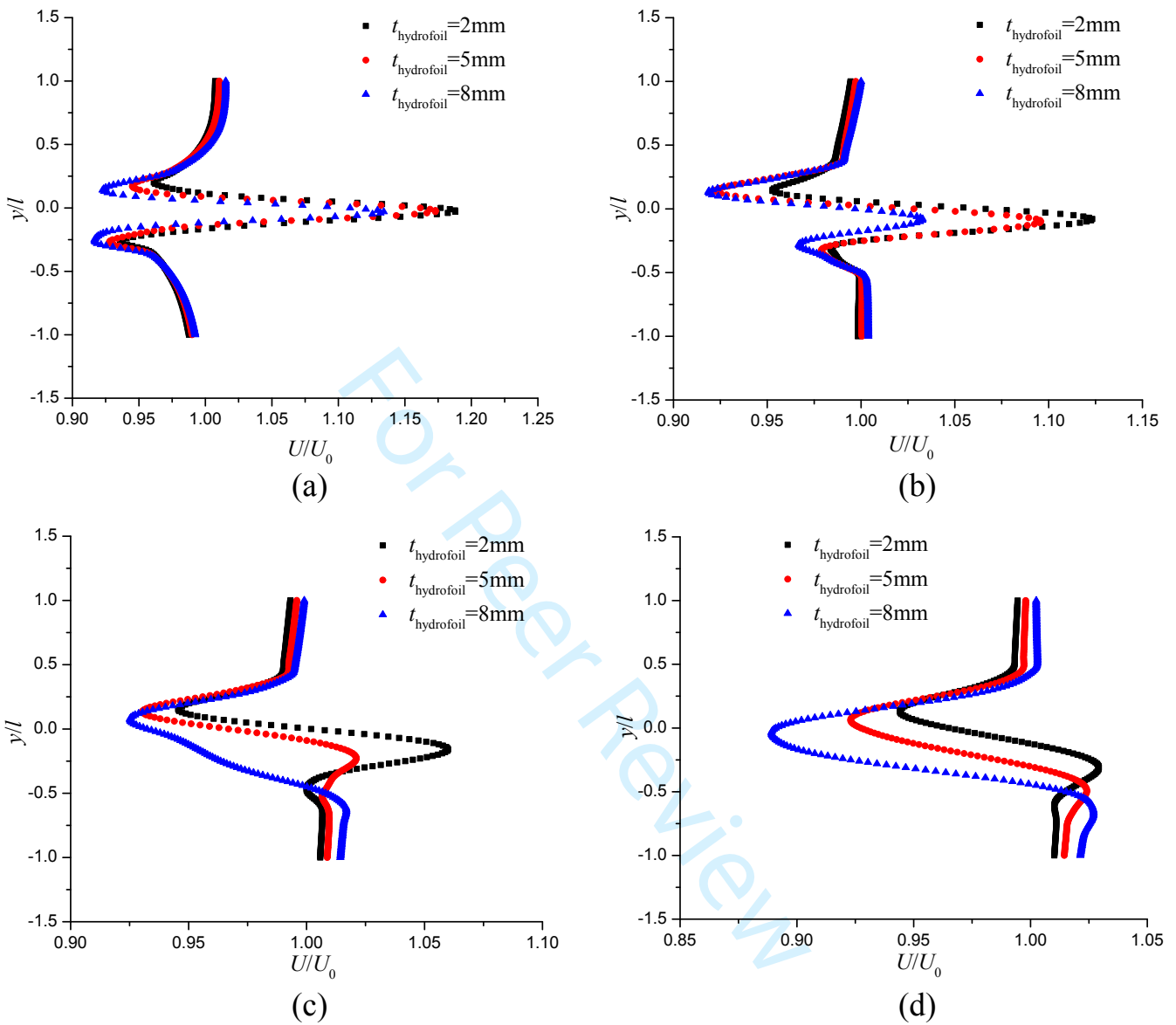
Fig.22 Mean velocity profiles in the wake region. (a) x/c=1.33; (b) x/c=2.67; (c) x/c=4; (d) x/c=5.33; (e) x/c=6.67.

5. Concluding remarks and future work

The SST $\gamma - \widetilde{Re}_\theta$ transition model was employed to simulate the two-dimensional flows around the bio-inspired pitching hydrofoils, with special emphasis on the effect of the pitching amplitude, reduced frequency, Reynolds number, hydrofoil shape and thickness on the global performance and unsteady vortical flows. The main conclusions are listed as follows:

(1) For the cases with relatively small pitching amplitudes, the mean lift coefficients increase with the reduced frequency. As the pitching amplitude increases, the mean lift coefficient improves initially and then drops obviously at high reduced frequency, as well as the drag coefficient. The lift coefficient variation in a cycle is ascribed to the pressure change on the aft surface with smooth curvature, depending on the oscillating motion significantly. Increasing the reduced frequency makes the drag coefficient change from the drag to thrust, and deflects the wake trajectory.

(2) The Reynolds number increases the mean lift coefficient and reduces the drag coefficient, which is also closely associated with the pressure change on the surface with smooth curvature. The wake morphology also changes with the Reynolds number, especially at low Reynolds number.

(3) The mean lift coefficient of hydrofoil A is much larger than hydrofoil B, especially at high reduced frequency. Moreover, the frequency in the hollows near the hydrofoil leading edge and in the wake region is nearly the same for two hydrofoils, which only depends on the pitching frequency. However, in the second

40

and third hollows, hydrofoil B has less sub-frequency with low energy, due to the relatively stable trapped vortices. Simultaneously, the wake transition from thrust-indicative to drag-indicative profile is more evident for hydrofoil A, indicating that the mean drag coefficient of hydrofoil B is smaller.

(4) By the comparison, it seems that with the increase of the hydrofoil thickness, the mean lift coefficient has improved a lot, specially from t=5mm to 8mm. However, the thin hydrofoil can generate the high lift/drag ratio, which can provide some guides to the designer for choosing an appropriate hydrofoil shape. In addition, it is observed that the difference of lift coefficient among three hydrofoils with different thicknesses is induced by the pressure change on the upper surface, especially after the second protrusion of hydrofoil A where induced vortex and separation vortex coexist. Furthermore, the hydrofoil with the thickness of 2mm has a slow wake transition, which is responsible for the relatively low drag coefficient.

It can be seen that there exits massive flow separation around the corrugated hydrofoils compared with the smooth hydrofoils, which makes the challenge to the RANS-based models. In addition, the drag coefficient has the considerable variations with the working conditions and geometry change, thus, it is quite necessary to use some high-resolution turbulence models, such as improved delayed detached eddy (IDDES) and large eddy simulation (LES), to reproduce the separated flows and unsteady wakes in the future work.

Acknowledgement

Nomenclature

Symbol quantity

ρ=density of the working fluids (kg/m^3)

k=turbulent kinetic energy (m^2/s^2)

u=velocity (m/s)

P_k=production of turbulent kinetic energy (m^2/s^3)

D_k=destruction term (m^2/s^3)

μ=dynamic viscosity (Pa.s)

μ_t=dynamic eddy viscosity (Pa.s)

ω=specific dissipation rate (s^{-1})

Cd_ω=cross-diffusion term

S=strain rate magnitude (s^{-1})

F_2=blending function

γ=intermittency

$\widetilde{Re}_{\theta t}$=momentum thickness Reynolds number

P_γ=production term of the intermittency equation

E_k=destruction term of the intermittency equation

$P_{\theta t}$=production term of the momentum thickness Reynolds number

γ_{eff}=effective intermittency

c=chord length (m)

Re=Reynolds number ($Re=cU_0/v$)

v=kinematic viscosity (m^2/s)

θ=pitch angle ($^\circ$)

θ_0=pitching amplitude ($^\circ$)

U_0=inlet velocity (m/s)

f=pitching frequency (Hz)

k_{red}=reduced frequency

y^+=non-dimensional distance from the wall

F_l=lift force (N)

F_d=drag force (N)

C_l=lift coefficient

C_d=drag coefficient

T=pitching period (s)

$t_{hydrofoil}$=hydrofoil thickness (m)

42

p=pressure (Pa)

C_{p}=pressure coefficient

ω_{z}=spanwise vorticity (s^{-1})

References

[1] Tseng, C. C., & Hu, H. A. (2016). Flow dynamics of a pitching foil by Eulerian and Lagrangian viewpoints. *AIAA Journal*, *54*(2), 712-727.

[2] Tseng, C. C., & Cheng, Y. E. (2015). Numerical investigations of the vortex interactions for a flow over a pitching foil at different stages. *Journal of Fluids and Structures*, *58*, 291-318.

[3] Ducoin, A., Astolfi, J. A., Deniset, F., & Sigrist, J. F. (2009). Computational and experimental investigation of flow over a transient pitching hydrofoil. *European Journal of Mechanics-B/Fluids*, *28*(6), 728-743.

[4] Menter, F. R., Langtry, R. B., Likki, S. R., Suzen, Y. B., Huang, P. G., & Völker, S. (2006). A correlation-based transition model using local variables—part I: model formulation. *Journal of Turbomachinery, 128*, 413-422.

[5] Menter, F. R., Langtry, R., & Völker, S. (2006). Transition modelling for general purpose CFD codes. *Flow, Turbulence and Combustion*, *77*(1-4), 277-303.

[6] Zhang, M., Wu, Q., Wang, G., Huang, B., Fu, X., & Chen, J. (2020). The flow regime and hydrodynamic performance for a pitching hydrofoil. *Renewable Energy*, *150*, 412-427.

[7] Moubogha, J. M., Ehrenstein, U., & Astolfi, J. A. (2017). Forces on a pitching plate: An experimental and numerical study. *Applied Ocean Research*, *69*, 27-37.

[8] Huang, B., Ducoin, A., & Young, Y. L. (2013). Physical and numerical investigation of cavitating flows around a pitching hydrofoil. *Physics of Fluids*, *25*(10), 102109 (1-27).

[9] Wang, S., Ingham, D. B., Ma, L., Pourkashanian, M., & Tao, Z. (2012). Turbulence modeling of deep dynamic stall at relatively low Reynolds number. *Journal of Fluids and Structures*, *33*, 191-209.

[10] Martinat, G., Braza, M., Hoarau, Y., & Harran, G. (2008). Turbulence modelling of the flow past a pitching NACA0012 hydrofoil at 10^5 and 10^6 Reynolds numbers. *Journal of Fluids and Structures*, *24*(8), 1294-1303.

[11] Wang, S., Ingham, D. B., Ma, L., Pourkashanian, M., & Tao, Z. (2010). Numerical investigations on dynamic stall of low Reynolds number flow around oscillating hydrofoils. *Computers & Fluids*, *39*(9), 1529-1541.

43

[12] Singh, K., & Páscoa, J. C. (2019). Numerical modeling of stall and poststall events of a single pitching blade of a cycloidal rotor. *Journal of Fluids Engineering*, *141*(1), 011103 (1-16).

[13] Ho, W. H., & New, T. H. (2017). Unsteady numerical investigation of two different corrugated hydrofoils. *Proceedings of the Institution of Mechanical Engineers, Part G: Journal of Aerospace Engineering*, *231*(13), 2423-2437.

[14] Hu, H., & Tamai, M. (2008). Bioinspired corrugated hydrofoil at low Reynolds numbers. *Journal of Aircraft*, *45*(6), 2068-2077.

[15] Murphy, J. T., & Hu, H. (2010). An experimental study of a bio-inspired corrugated hydrofoil for micro air vehicle applications. *Experiments in Fluids*, *49*(2), 531-546.

[16] New, T. H., Chan, Y. X., Koh, G. C., Hoang, M. C., & Shi, S. (2014). Effects of corrugated aerofoil surface features on flow-separation control. *AIAA Journal*, *52*(1), 206-211.

[17] Levy, D. E., & Seifert, A. (2009). Simplified dragonfly hydrofoil aerodynamics at Reynolds numbers below 8000. *Physics of Fluids*, *21*(7), 071901 (1-17).

[18] Flint, T. J., Jermy, M. C., New, T. H., & Ho, W. H. (2017). Computational study of a pitching bio-inspired corrugated hydrofoil. *International Journal of Heat and Fluid Flow*, *65*, 328-341.

[19] Menter, F. R., Kuntz, M., & Langtry, R. (2003). Ten years of industrial experience with the SST turbulence model. *Turbulence, Heat and Mass Transfer*, *4*(1), 625-632.

[20] Ramsay, R. F., Hoffman, M. J., & Gregorek, G. M. (1995). Effects of grit roughness and pitch oscillations on the S809 airfoil (No. NREL/TP-442-7817). National Renewable Energy Lab.(NREL), Golden, CO (United States).

[21] Hosseinjani, A. A., & Ashrafizadeh, A. (2015). Numerical simulation of the wake structure and thrust/lift generation of a pitching hydrofoil at low Reynolds number via an immersed boundary method. *Journal of Aerospace Technology and Management*, *7*, 334-350.

44